RSC Advances

PAPER

View Article Online
View Journal | View Issue

Cite this: *RSC Adv.*, 2025, **15**, 48171

Antibacterial and antibiofilm activity of green synthesized Mg-doped CeO_2 nanoparticles using *Actinidia deliciosa* peel extract

Nibedita Nayak,[a] Uday Suryakanta,[b] Swatilekha Das,[b] Dindyal Mandal [b] and Tapas Ranjan Sahoo *[a]

This study reports the green synthesis of cerium oxide (CeO_2) and magnesium-doped cerium oxide (Mg-doped CeO_2) nanoparticles by a sol–gel method using kiwi (*Actinidia deliciosa*) peel extract as a natural reducing and stabilizing agent. The synthesized nanoparticles were thoroughly characterized using a range of techniques including XRD, FTIR spectroscopy, FESEM, HRTEM, BET analysis, PL spectroscopy, Raman spectroscopy and UV-Vis spectroscopy. These analyses confirmed the successful synthesis of nanoparticles with well-defined crystalline structures and appropriate morphology. The antibacterial potential of the nanoparticles was evaluated against pathogenic bacteria including methicillin-resistant *Staphylococcus aureus*, *Escherichia coli*, and *Pseudomonas aeruginosa*. Results demonstrated that both nanoparticles exhibited significant antibacterial activity, with Mg-doped CeO_2 nanoparticles showing the most potent antibacterial activity. The antibacterial activity of Mg-doped CeO_2 nanoparticles was evaluated by measuring the zone of inhibition, which was found to be 12 mm for *Staphylococcus aureus*, 15 mm for *Escherichia coli*, and 14 mm for *Pseudomonas aeruginosa*. Compared with the undoped CeO_2 nanoparticles, the Mg-doped CeO_2 nanoparticles exhibited enhanced antibacterial efficacy, with minimum inhibitory concentration (MIC) values of 62.5 μg mL^{-1} for MRSA (*S. aureus*), 15.63 μg mL^{-1} for *E. coli*, and 15.63 μg mL^{-1} for *P. aeruginosa*. Furthermore, the synthesized Mg-doped CeO_2 nanoparticles demonstrated significant biofilm inhibition activity against methicillin-resistant *Staphylococcus aureus* (MRSA). The observed antibacterial activity was further supported by reactive oxygen species (ROS) generation, indicating ROS-mediated bactericidal action as the underlying mechanism. These findings highlight the potential of Mg-doped CeO_2 nanoparticles as effective antibacterial agents, offering a promising approach for the treatment of bacterial infections including those caused by antimicrobial-resistant strains.

Received 8th October 2025
Accepted 21st November 2025

DOI: 10.1039/d5ra07686b

rsc.li/rsc-advances

1. Introduction

The alarming rise in antibacterial resistance (ABR) poses a significant threat to global health, rendering many existing antibiotics ineffective against pathogenic bacterial strains. Bacterial infections that were once curable are now evolving into life-threatening diseases, leaving healthcare systems overwhelmed and millions of lives at risk.[1,2] The overuse and misuse of antibiotics have accelerated the evolution of resistant pathogens, creating a silent epidemic that threatens to undo decades of medical advancements.[3] Among the most prevalent bacterial species contributing to nosocomial and community-acquired infections are *Staphylococcus aureus* (a Gram-positive bacterium) and *Escherichia coli* and *Pseudomonas aeruginosa* (Gram-negative bacteria).[4,5] These pathogens are particularly concerning due to their adaptability and ability to develop multiple resistance mechanisms including biofilm formation, efflux pump activation, enzymatic degradation of antibiotics, and horizontal gene transfer of resistance determinants.[6,7] Biofilm formation, in particular, enables bacteria to shield themselves from host immune responses and antimicrobial agents, leading to chronic infections and treatment failures.[8] In *Staphylococcus aureus*, biofilms are stabilized by an extracellular polymeric substance (EPS), notably polysaccharide intercellular adhesin (PIA), synthesized by the icaADBC operon, which enhances bacterial adhesion and impedes antibiotic penetration.[9] Additionally, *E. coli* utilizes the AcrAB-TolC efflux pump, a tripartite system from the RND family, to expel antibiotics such as β-lactams and fluoroquinolones, thereby lowering the intracellular drug levels and contributing to multidrug resistance.[10] These resistance strategies not only weaken the effectiveness of conventional antibiotics but also complicate treatment outcomes. Consequently, there is a pressing need to

[a]*Department of Chemistry, School of Applied Sciences, KIIT deemed to be University, Bhubaneswar 24, Odisha, India. E-mail: trsahoofch@kiit.ac.in*
[b]*School of Biotechnology, KIIT deemed to be University, Bhubaneswar 24, Odisha, India*

explore alternative therapeutic strategies, such as nanoparticle-based antibacterial agents, which can overcome these mechanisms through size-dependent membrane interactions and reactive oxygen species (ROS)-mediated bacterial damage.

Furthermore, Gram-negative bacteria such as *E. coli* and *P. aeruginosa* possess double-layered cell membrane, which serves as a formidable barrier to many antibiotics, contributing to their resistance and persistence in diverse environments including clinical settings,[11] and *S. aureus* is notorious for its methicillin-resistant strain, which have become a leading cause of hard-to-treat skin, soft tissue, and bloodstream infections.[12] The combined effect of these resistance strategies significantly limits the efficacy of existing antibiotics, leaving healthcare providers with limited therapeutic options, particularly for immunocompromised patients. Addressing this urgent issue requires novel and sustainable antimicrobial strategies that overcome bacterial resistance while minimizing environmental and health risks.[13,14]

Nanotechnology has emerged as a promising approach in combating antimicrobial resistance due to the unique physicochemical properties of nanoparticles (NPs), including their high surface area-to-volume ratio and versatile biological functionalities.[15,16] Among various nanomaterials, metal oxide nanoparticles (MONPs) have garnered considerable attention for their broad-spectrum antibacterial activity, biocompatibility, and eco-friendly synthesis potential.[17] Cerium oxide nanoparticles (CeO_2 NPs), in particular, exhibit dual redox properties owing to their ability to transition between Ce^{3+} and Ce^{4+} oxidation states. This redox cycling enables cerium oxide to generate reactive oxygen species (ROS), disrupt bacterial membranes, and interfere with cellular components, ultimately leading to bacterial cell death.[18,19] Pristine CeO_2 NPs exhibit significant antibacterial performance due to their surface stability and intrinsic redox activity.

However, to further enhance the antibacterial efficacy, Mg doping has been studied as a strategic approach to modulate the oxygen vacancy concentration and improve ROS generation, thereby amplifying the antimicrobial effect.[20–22] Magnesium-doped CeO_2 nanoparticles introduce additional oxygen vacancies and active sites, improving ROS generation and bacterial membrane disruption.[23,24] Magnesium itself is recognized for its antimicrobial properties, biocompatibility, and physiological relevance, contributing to enhanced oxidative stress induction and metal ion toxicity in bacterial cells.[25–27]

The synthesis method employed for nanoparticle fabrication plays a critical role in determining their size, morphology, oxidation states, and biological activity.[28] Conventional methods including thermal decomposition, precipitation, and hydrothermal synthesis often require harsh reaction conditions, toxic reagents, and complex processes that raise environmental and safety concerns.[29] In contrast, green synthesis approaches offer a sustainable alternative by utilizing plant extracts, which are rich in bioactive compounds such as polyphenols, flavonoids, tannins, and alkaloids, as natural reducing and stabilizing agents.[30,31] Plant-based synthesis not only eliminates the need for hazardous chemicals but also improves nanoparticle biocompatibility, rendering them suitable for biomedical and environmental applications.[32]

Recent studies have demonstrated the successful use of plant extracts such as *Moringa oleifera*, *Camellia sinensis*, and *Acacia concinna* in the synthesis of metal and metal oxide nanoparticles with enhanced antioxidant and antibacterial properties.[33,34] Khadar *et al.* synthesized Co-doped CeO_2 NPs by a hydrothermal method and studied antibacterial activity against pathogenic bacteria such as *Escherichia coli*, *Staphylococcus aureus*, *Bacillus Cereus* and *Salmonella typhi*[35], Maleki *et al.* synthesized Ag-doped CeO_2 nanoparticles *via* a green bioprocess by water extract of *Salvia* seeds as a capping agent and used the prepared NPs to study antibacterial activity against pathogenic bacteria like *Staphylococcus aureus* and *Pseudomonas aeruginosa*,[36] Norbert *et al.* investigated phyto-synthesized Cu-doped CeO_2 NPs against pathogenic bacteria *Escherichia coli*, *Staphylococcus aureus*, and *Bacillus cereus*.[37]

In this study, *Actinidia deliciosa* (kiwi) peel extract was employed as a green reducing and stabilizing agent for the synthesis of CeO_2 and Mg-doped CeO_2 nanoparticles. Unlike many conventional plant extracts, *Actinidia deliciosa* peel is particularly rich in unique and abundant polyphenols such as quercetin, catechin, and gallic acid, along with a high content of organic acids such as citric and ascorbic acid.[38,39] These bioactive compounds exhibit stronger redox potential and more effective chelation ability with Ce^{4+} ions, which significantly enhances the rate and uniformity of nanoparticle formation during the sol–gel reaction. The presence of these molecules promotes simultaneous reduction and stabilization, leading to improved control over nucleation, smaller crystallite sizes, and better particle dispersion. Mechanistically, the kiwi peel extract offers a dual function: (i) redox-active molecules facilitate the bio-reduction of Ce^{4+} to Ce^{3+} and (ii) hydroxyl- and carboxyl-rich phytochemicals act as natural capping agents, preventing agglomeration and ensuring high colloidal stability. Utilizing kiwi peel extract not only valorizes agricultural waste but also promotes an eco-friendly and sustainable synthesis route that minimizes environmental impact.[40] Furthermore, this green approach is cost-effective due to the low cost and easy accessibility of the raw material, making it a practical alternative for large-scale production. Overall, the use of kiwi peel extract supports sustainable development goals by integrating waste valorization with green chemistry principles, aligning well with efforts to reduce chemical hazards and promote environmentally benign manufacturing processes.[41]

To evaluate their antibacterial performance, the synthesized nanoparticles were tested against three clinically significant bacterial strains *Staphylococcus aureus* (Gram-positive), and *Escherichia coli* and *Pseudomonas aeruginosa* (Gram-negative). These bacterial strains were chosen due to their medical importance and increasing resistance to conventional antibiotics.[42] *E. coli* and *S. aureus* are leading causative agents of infections such as urinary tract infections, sepsis, and skin infections, while *P. aeruginosa* is an opportunistic pathogen known for causing severe infections in immunocompromised patients and for its remarkable ability to develop multidrug resistance.[43]

Furthermore, the systematic evaluation of antibacterial activity provides critical insights into the role of magnesium doping in enhancing the efficacy of CeO_2 nanoparticles. The comparative analysis with CeO_2 nanoparticles highlights the relative performance of these materials and their potential applications as antibacterial agents.

This study represents an eco-friendly and sustainable approach for synthesizing CeO_2 and Mg-doped CeO_2 nanoparticles by a sol–gel method using *Actinidia deliciosa* (kiwi) peel extract. The synthesized nanoparticles were thoroughly characterized, and their antibacterial properties were evaluated against clinically relevant bacterial strains. The findings not only demonstrate the significant potential of these green-synthesized nanoparticles in combating antimicrobial resistant pathogens but also highlight their role in addressing global challenges related to antimicrobial resistance and environmental sustainability.

2. Experimental

2.1. Materials

Ammonium cerium(IV) nitrate (99.9% purity, Merck), magnesium nitrate(II) hexahydrate (99% purity, Merck), crystal violet (95% purity, HiMedia), 2,7-dichlorodihydrofluorescein diacetate (98% purity, Invitrogen), Luria–Bertani (LB) broth and LB agar (HiMedia), glutaraldehyde, ethanol and other analytical grade reagents were used without further purification.

2.2. Synthesis of CeO_2 and Mg-doped CeO_2 nanoparticles

The synthesis of CeO_2, MgO, and 6% Mg-doped CeO_2 nanoparticles was performed by a sol–gel method with *Actinidia deliciosa* (kiwi) peel extract as a natural reducing and stabilizing agent (Fig. 1). Fresh kiwi fruits were procured from the local market, thoroughly washed with distilled water, and peeled. The peels were shade-dried at ambient temperature for 72 hours and then ground into a fine powder using a domestic mixer grinder. Then, 10 grams of this powder was added to 100 mL of distilled water and heated at 60 °C for 1 hour with continuous stirring. The resulting mixture was filtered using Whatman filter paper, and the extract was stored at 4 °C for further use. After that, 20 mL of the prepared kiwi peel extract was stirred at 90 °C for 30 minutes. Then, 4 g of ammonium cerium(IV) nitrate was added under continuous stirring at 400 rpm. The solution was maintained at 90 °C for 6 hours until a gel-like mass formed. This gel was dried at 100 °C in a hot-air oven and subsequently calcined at 400 °C for 2 hours in a muffle furnace to obtain cerium oxide nanoparticles. MgO NPs were also synthesized similarly by the sol–gel method taking magnesium nitrate(II) hexahydrate as the precursor and kiwi peel extract as the reducing and stabilizing agent. To synthesize 6% Mg-doped CeO_2 nanoparticles, magnesium nitrate(II) hexahydrate was added along with ammonium cerium(IV) nitrate (99.9%, Merck) in the required stoichiometric ratio. The solution was stirred at 400 rpm and 90 °C for 6 hours, following the same procedure as for pure CeO_2. The resulting gel was then dried at 100 °C, and the solid product was calcined at 400 °C for 2 hours in a muffle furnace to obtain Mg-doped CeO_2 nanoparticles.

2.3. Instrumentation and methodology

These as-synthesized nanoparticles were examined by several characterization methods such as XRD, FESEM, HRTEM, FTIR spectroscopy, Raman spectroscopy, PL spectroscopy and UV-Vis spectroscopy, after successful synthesis. The nanomaterials were subjected to CuKα radiation from 10° to 100° using a Bruker advance X-ray diffractometer. The Debye–Scherrer equation was used for estimating the average crystallite size of particles based on the XRD data.

$$D = \frac{K\lambda}{\beta \cos \theta} \quad (1)$$

where D represents the average crystallite size, K is a constant close to unity, λ denotes the X-ray wavelength (0.15418 nm), and β is the breadth of diffraction that equals FWHM. The Williamson Hall (W–H) method is based on the following equation:

$$\beta \cos \theta = \frac{k\lambda}{D} + 4\varepsilon \sin \theta \quad (2)$$

where β is the full width at half maximum (FWHM) of the diffraction peak, θ is the Bragg angle, k is the shape factor (typically 0.9), λ is the X-ray wavelength, D is the average crystallite size, and ε is the micro strain. The morphology of materials was investigated using a ZEISS field emission scanning electron microscope. Furthermore, HRTEM analysis was

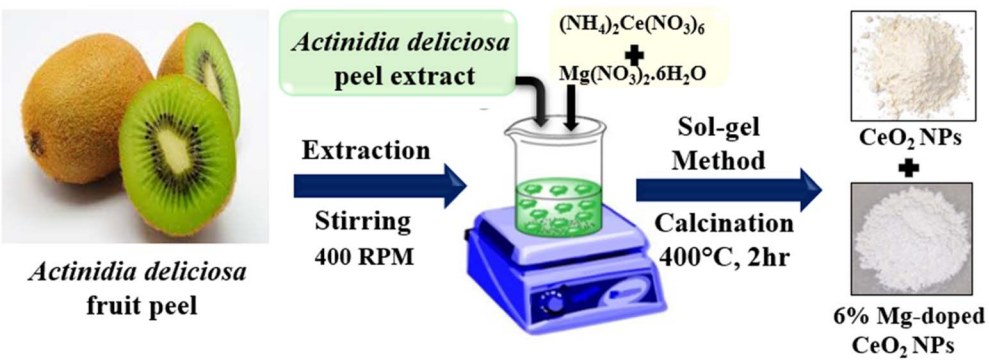

Fig. 1 Schematic of the green synthesis of CeO_2 and Mg-doped CeO_2 NPs by a sol–gel method using *Actinidia deliciosa* peel extract.

performed using a HRTEM JEOL/JEM 2100 instrument. To determine the purity of the as-synthesized materials, FTIR spectra were recorded using a Bruker ALPHA II FTIR spectrophotometer. A Renishaw UK spectrometer was used to perform Raman spectroscopy in red diode laser 633. A JASCO V-770 UV-Visible spectrophotometer was used to record UV-Visible spectra of the samples at room temperature.

2.4. Bacterial strains and growth conditions

Methicillin-resistant *Staphylococcus aureus* (MRSA, ATCC 43300), *Pseudomonas aeruginosa* (PAO1), and *Escherichia coli* (ATCC 35218) were procured from the American Type Culture Collection (ATCC) and maintained under laboratory conditions. The bacterial strains were cultured in Luria–Bertani (LB) broth at 37 °C and harvested during mid-logarithmic growth phase for use in all subsequent experiments. This standardized preparation ensured the physiological consistency of bacterial cells across all experimental setups.

2.5. Antibacterial activity

Bacterial cultures were grown overnight in a Luria–Bertani (LB) medium at 37 °C under shaking conditions to promote optimal growth. The cultures were centrifuged at 5000×*g* for 5 minutes to pellet the cells. The resulting pellets were washed with sterile phosphate-buffered saline (PBS, pH 7.4) and resuspended in a fresh LB medium to achieve standardized bacterial concentration. LB agar plates were prepared, and aliquots (100 μL) of the standardized bacterial suspension were evenly spread across the agar surface using a sterile glass spreader to ensure uniform distribution. Wells of consistent diameter were carefully bored into the agar using a sterile gel borer under aseptic conditions. CeO_2, Mg-doped CeO_2, and MgO nanoparticle solutions were prepared from a 1 mg mL^{-1} stock solution and dispensed into the wells. Kanamycin (50 μg mL^{-1}), a standard antibiotic, was included as a positive control. Equal volumes of nanoparticle solutions and kanamycin were added to each well to maintain consistency across samples. The plates were incubated at 37 °C for 24 hours. Following incubation, the antibacterial efficacy of the nanoparticles was determined by measuring the diameter of the zone of inhibition (ZOI) around each well using a ruler. The ZOI values were recorded and analyzed to assess the comparative activity of the nanoparticle formulations and the antibiotic control.

2.6. Minimum inhibitory concentration

Bacterial strains (*Staphylococcus aureus*, *Pseudomonas aeruginosa* and *Escherichia coli*) were grown in Luria–Bertani (LB) broth at 37 °C to mid-logarithmic phase. Cultures were adjusted to a final density of 1×10^6 CFU mL^{-1} in fresh LB broth to standardize initial inoculum. A 96-well polystyrene microtiter plate was used for the OD-based MIC determination assay. Each well was filled with 100 μL of bacterial suspension and 100 μL of nanomaterial (cerium oxide, magnesium oxide and Mg-doped CeO_2 NPs) suspension at different concentrations (500 μg mL^{-1}, 250 μg mL^{-1}, 125 μg mL^{-1}, 62.5 μg mL^{-1}, 31.25 μg mL^{-1}, 15.625 μg mL^{-1}, 7.81 μg mL^{-1}, 3.90 μg mL^{-1}, 1.95 μg mL^{-1}, and 0.97 μg mL^{-1}), and kanamycin was taken as an antibiotic control at different concentrations (50 μg mL^{-1}, 25 μg mL^{-1}, 12.5 μg mL^{-1}, 6.25 μg mL^{-1}, 3.125 μg mL^{-1}, 1.56 μg mL^{-1}, 0.78 μg mL^{-1}, 0.390 μg mL^{-1}, 0.195 μg mL^{-1}, and 0.097 μg mL^{-1}). Positive control wells contained a bacterial suspension without any nanomaterial to monitor regular growth. Negative control wells contained only LB broth without bacteria to ensure sterility. The plates were incubated at 37 °C for 12 and 24 hours under shaking conditions at 150 rpm to ensure uniform exposure. After incubation, the optical density (OD) was measured at 600 nm using a microplate reader to determine the bacterial growth. The OD readings of each well were compared with the positive control to evaluate growth inhibition.

2.7. Bacterial cell morphology analysis

The cultures of *Staphylococcus aureus*, *Escherichia coli*, and *Pseudomonas aeruginosa* at a concentration of 1×10^6 CFU mL^{-1} were treated with CeO_2, MgO, and Mg-doped CeO_2 NPs at a final concentration of 25 μg mL^{-1}. Untreated bacterial cells served as the control. All samples were incubated at 37 °C for 12 hours in a shaking incubator to ensure uniform exposure. Following incubation, bacterial cells were harvested by centrifugation at 8000 rpm for 5 minutes and washed three times with 1 × PBS to remove residual media and treatment agents. Cell smears were prepared on aluminum foil and fixed with a 2.5% glutaraldehyde solution overnight at 4 °C. After fixation, the samples were washed three times with PBS to eliminate excess fixative. Subsequently, the cells underwent dehydration using an ascending ethanol gradient (30%, 50%, 70%, 90%, and 100%), with each step lasting 10 minutes. The final dehydration step in absolute ethanol ensured complete removal of moisture as the sample was subjected to drying in a laminar air flow hood. The dehydrated samples were mounted onto stubs and coated with a thin layer of gold using a sputter coater. The prepared samples were analyzed using a scanning electron microscope (SEM) to evaluate morphological alterations. The observations of treated and untreated bacterial cells were compared to assess the structural changes induced by the nanomaterials.

2.8. Biofilm inhibition assay

A crystal violet assay was conducted to evaluate the biofilm inhibition properties of Mg-doped CeO_2 nanoparticles against methicillin-resistant *Staphylococcus aureus* (MRSA). A log-phase culture of *S. aureus* (1×10^7 CFU mL^{-1}) was prepared and co-incubated with different concentrations of Mg–CeO_2 (5 μg mL^{-1}, 15 μg mL^{-1}, 25 μg mL^{-1}, 50 μg mL^{-1}, and 100 μg mL^{-1}) in a 96-well plate. The cultures were incubated under static conditions at 37 °C for 24 hours to promote biofilm formation. Following incubation, wells were gently washed three times with 1 × PBS to remove non-adherent and dead cells. The plates were then dried for 1 hour at 37 °C. Subsequently, 200 μL of 0.1% crystal violet solution was added to each well and incubated for 1 hour at 37 °C to stain the biofilms. Excess dye was removed by washing with 1× PBS, and the plate was again dried for 1 hour. To solubilize the bound stain, 200 μL of 33% (v/v) glacial acetic acid was added to each well. The absorbance

was measured at 590 nm using a Multiskan Microplate Photometer. The percentage of biofilm inhibition was calculated using the following equation:

$$\left[\%\ \text{Biomass} = \frac{\text{Abs}^{590\text{nm}}\ (\text{treatment}) - \text{Abs}^{590\text{nm}}(\text{blank})}{\text{Abs}^{590\text{nm}}\ (\text{control}) - \text{Abs}^{590\text{nm}}(\text{blank})} \times 100\right] \quad (3)$$

2.9. Reactive oxygen species

The fluorescent dye 2,7-dichlorofluorescein diacetate (DCF-DA) was employed to detect intracellular reactive oxygen species (ROS) generation following treatment with CeO_2 and Mg–CeO_2 NPs. *Staphylococcus aureus* (MRSA) cultures at a concentration of 1×10^6 CFU mL^{-1} were treated with CeO_2 and Mg-doped CeO_2 NPs at two concentrations (25 μg mL^{-1} and 50 μg mL^{-1}) for 5 hours at 37 °C. After treatment, both control and treated samples were collected and washed with 1× PBS to remove residual media and unbound nanoparticles. The resulting cell pellets were resuspended in 100 μL of 1× PBS. Subsequently, 10 μM of DCF-DA dye was added to each sample, followed by incubation in the dark for 15 minutes to allow intracellular ROS-mediated conversion of the dye to its fluorescent form. Excess dye was removed by centrifugation at 5000 rpm, and the resulting pellets were resuspended in 100 μL of 1× PBS. For microscopic analysis, 10 μL of each sample was placed onto a clean glass slide, covered with a coverslip, and examined using a fluorescence microscope (ZEISS Axiovert 5) with a green filter and a 40× objective lens. The fluorescence intensity was used as an indicator of intracellular ROS generation.

3. Results and discussion

3.1. Characterization

3.1.1. X-ray diffraction (XRD). The XRD spectra of the 6% Mg-doped CeO_2 and pure CeO_2 nanoparticles are illustrated in Fig. 2(a), demonstrating their nanocrystalline nature. All diffraction peaks are indexed to the crystal planes (111), (200), (220), (311), (222), (400), (331), (420), (442), and (511), which correspond to the cubic fluorite structure of CeO_2 NPs with the $Fm\bar{3}m$ space group. The absence of additional peaks suggests that the cubic phase remains the sole phase in both pure and Mg-doped CeO_2 nanoparticles. The MgO peaks indexed to the (111), (200), (220), (311), and (222) planes correspond to the face-centered cubic phase of MgO with an average crystallite size of 35 nm. Furthermore, as depicted in Fig. 2(b), the (111) peak of pure CeO_2 appears at 28.53°, while that of Mg-doped CeO_2 NPs shifts to 28.61°, confirming a shift toward higher diffraction angles.[44] To support this observation, the corresponding lattice spacing was calculated using Bragg's law. For pure CeO_2 NPs, the lattice spacing was found to be 3.124 Å, while for Mg-doped CeO_2 it decreased to 3.117 Å. This reduction in lattice space reflects the substitution of larger Ce^{4+} ions (1.01 Å) by smaller Mg^{2+} ions (0.72 Å), causing local lattice distortion and contraction. These quantitative results provide direct structural evidence of successful Mg^{2+} incorporation into the CeO_2 lattice.

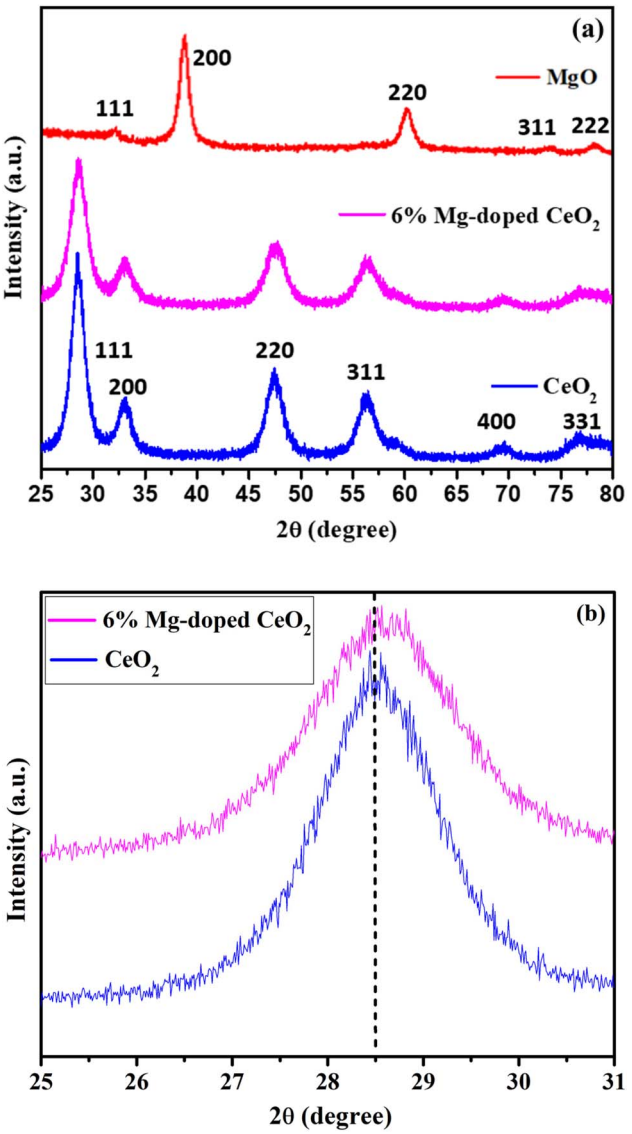

Fig. 2 (a) XRD pattern of CeO_2 NPs, 6% Mg-doped CeO_2 NPs, and MgO NPs. (b) Shift in the (111) peak due to doping with Mg.

The average crystallite size of the particles was calculated using Debye–Scherrer's formula. With the increase in Mg doping concentration from 0% to 6%, the average crystallite size decreased from 6.4 nm to 5 nm. This reduction is probably due to the lattice contraction induced by the replacement of Ce^{4+} with Mg^{2+} ions. The absence of secondary phases and the observed decrease in average crystallite size confirm the effective doping of Mg^{2+} ions into the CeO_2 host matrix.

The W–H plots for both pure CeO_2 and 6% Mg-doped CeO_2 nanoparticles are demonstrated in Fig. 3(a) and (b). From the linear fitting of the W–H plots, the slope of the fitted line corresponds to the micro strain present in the crystal lattice, whereas the intercept on the *y*-axis is used to estimate the average crystallite size of the nanoparticles. The calculated average crystallite size for pure CeO_2 nanoparticles is 6.2 nm,

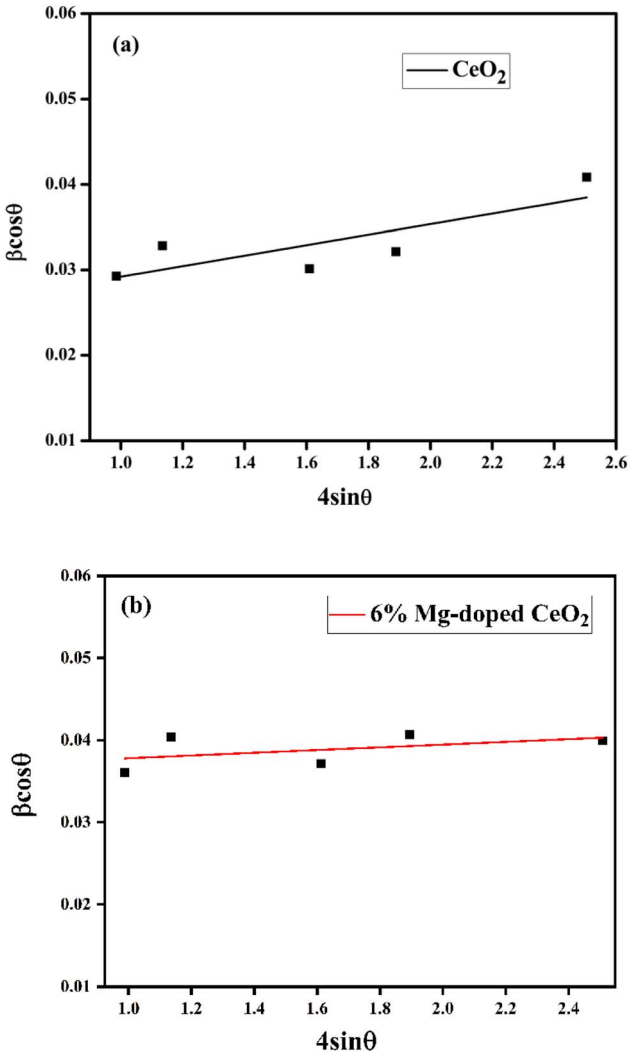

Fig. 3 Williamson–Hall plot for (a) CeO_2 NPs and (b) 6% Mg-doped CeO_2 NPs.

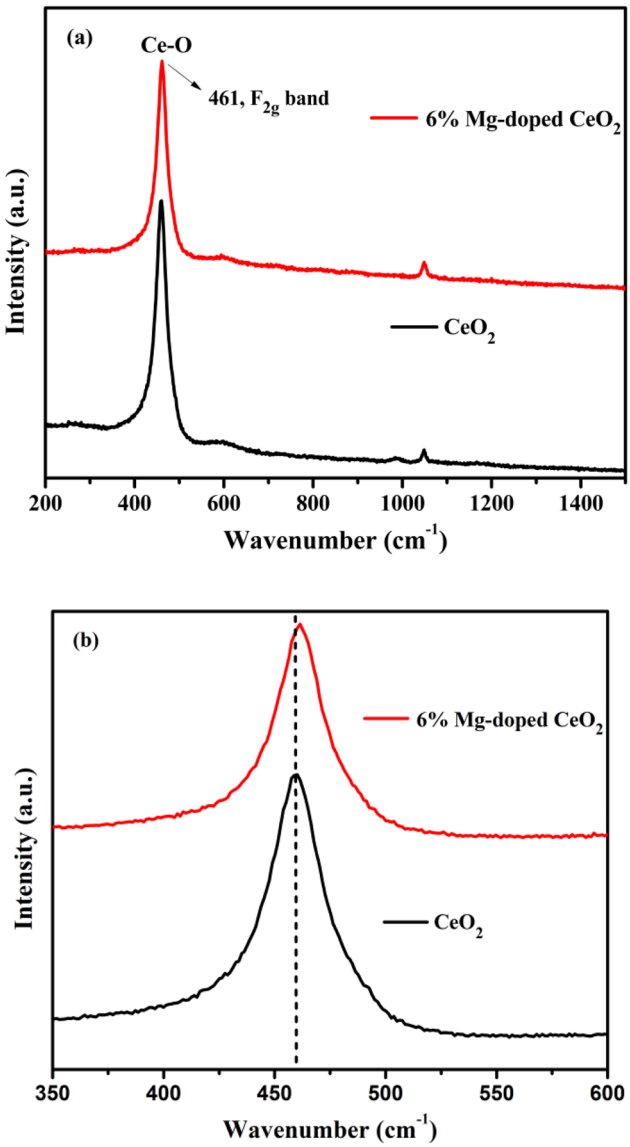

Fig. 4 (a) Raman spectra of CeO_2 NPs and 6% Mg-doped CeO_2 NPs and (b) shift in the F_{2g} peak due to doping with Mg.

and for 6% Mg-doped CeO_2 nanoparticles, it is 4.8 nm. The corresponding microstrain values are 0.0061 for pure CeO_2 and 0.0016 for 6% Mg-doped CeO_2 NPs. These results confirm that Mg doping leads to a reduction in lattice strain and a slight decrease in average crystallite size, supporting our earlier assertion that the XRD peak shifts are due to both lattice contraction and structural deformation. The observed decrease in lattice strain may influence the defect structure and surface reactivity of the nanoparticles, which could play a role in enhancing reactive oxygen species generation and improving interactions with bacterial membranes.

3.1.2. Raman spectroscopy. Raman spectroscopy was performed to evaluate the phase purity and structural properties of CeO_2 and 6% Mg-doped CeO_2 nanoparticles, providing insights into their vibrational characteristics and defect structures (Fig. 4(a)). The Raman spectra of CeO_2 and Mg-doped CeO_2 NPs exhibit a strong peak at 461 cm^{-1}, attributed to the F_{2g} vibrational mode of the cubic fluorite structure, arising from the symmetric stretching mode of the Ce–O_8 crystal unit in CeO_2.[45]

Upon doping with Mg, significant changes are observed, including peak shifting, broadening, and intensity reduction, of the F_{2g} mode (Fig. 4(b)), indicative of increased defect density, particularly oxygen vacancies and interstitial defects, introduced by the substitution of Ce^{4+} ions (1.01 Å) with smaller Mg^{2+} ions (0.72 Å). These defects modify the electronic and optical properties of the nanoparticles, enhancing their functional performance. The absence of peaks corresponding to MgO in the Mg-doped CeO_2 spectra confirms the successful incorporation of Mg into the CeO_2 lattice without forming separate MgO phases. The small peak at 1051 cm^{-1} is attributed to carbonate species (CO_3^{2-}) adsorbed on the nanoparticle surface, resulting from CO_2 interaction with surface-active sites.

3.1.3. Fourier transform infrared (FT-IR) spectroscopy. The FTIR spectrum of the synthesized nanoparticles reveals multiple characteristic vibrational bands corresponding to

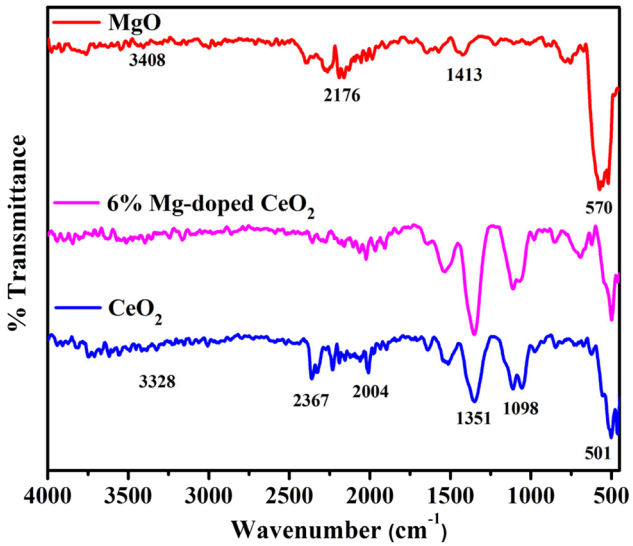

Fig. 5 FT-IR spectra of CeO_2 NPs, 6% Mg-doped CeO_2 NPs, and MgO NPs.

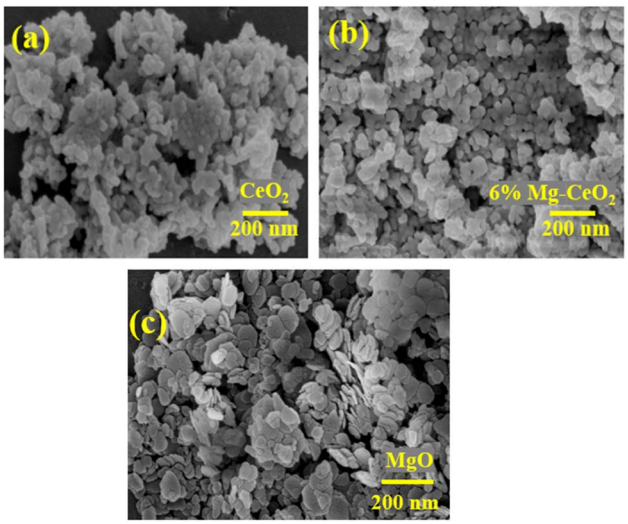

Fig. 6 FESEM images of (a) CeO_2 NPs, (b) 6% Mg-doped CeO_2 NPs, and (c) MgO NPs.

various functional groups associated with both the inorganic matrix and residual organic moieties from the green synthesis process (Fig. 5). A broad absorption band centered around 3511 cm^{-1} is attributed to the O–H stretching vibrations of surface hydroxyl groups, physisorbed water molecules, and phenolic compounds derived from the plant extract. The band observed at 1637 cm^{-1} is associated with the bending vibration of H–O–H from molecular water, with potential overlap from the C=O stretching vibrations of carboxylic or carbonyl-containing compounds originating from phytochemicals. Notably, the band at 1525 cm^{-1} corresponds to the Amide II band that suggests the presence of proteins or amino-containing compounds from the plant extract, while the band at 1343 cm^{-1} is attributed to the C–H bending vibrations, indicative of residual aliphatic or aromatic organic moieties acting as natural capping agents. Additionally, the doublet at 1038 and 1109 cm^{-1} corresponds to C–O stretching vibrations, which are typical of alcohols, ethers, or glycosidic linkages found in polyphenols and the band at 2367 cm^{-1} is more accurately attributed to the asymmetric stretching mode of atmospheric CO_2, which may have been introduced as a contaminant during FTIR analysis. In addition, the band at 2004 cm^{-1} may result from the combination or overtone bands arising from complex vibrational couplings in organic molecules, or potentially due to adsorbed carbon monoxide (CO) species interacting with surface metal atoms of the nanoparticles. Additionally, a weak absorption near 700 cm^{-1} is indicative of metal oxygen stretching vibrations, and the intense band at 501 cm^{-1} is characteristic of the Ce–O stretching mode in the cubic fluorite structure of CeO_2, thereby confirming the successful formation of cerium oxide nanoparticles.[46] The FTIR spectra of MgO nanoparticles displayed a broad band around 570 cm^{-1}, attributed to the metal–oxygen bending vibration band, confirming the formation of Mg–O bonds. The band at 3408 cm^{-1} corresponded to the stretching frequency of the H–O–H bond, indicating the presence of adsorbed water molecules. Additionally, a broad peak near 2176 cm^{-1} was observed, which was ascribed to the C=O stretching frequency in CO_2. The small peaks near 1413 cm^{-1} are associated with the presence of organic residues, which likely serve as stabilizing agents on the surface of the MgO nanoparticles.

3.1.4. Field emission scanning electron microscopy (FESEM). Fig. 6(a–c) depict the FESEM micrographs of MgO, CeO_2, and 6% Mg-doped CeO_2 NPs, respectively, which thoroughly displayed the surface morphology of the materials. The FESEM images reveal the development of uniformly distributed spherical nanoparticles with irregular morphology across all samples, including pure CeO_2, MgO and Mg-doped CeO_2 NPs. The overall morphological behaviour of Mg-doped CeO_2 NPs resembles that of CeO_2 NPs, which indicates that the doping process did not significantly alter the fundamental shape and distribution of the nanoparticles. The doping process preserved the fundamental morphology, indicating that the incorporation of Mg did not disrupt the nanoparticle formation mechanism facilitated by the kiwi peel extract. The average grain size measured using the ImageJ software ranged from 45–60 nm for all samples, highlighting the uniformity of the synthesized nanoparticles.

3.1.5. Energy-dispersive X-ray spectroscopy (EDS) and elemental mapping. The energy-dispersive X-ray spectroscopy (EDS) analysis provides a detailed insight into the elemental composition of the synthesized CeO_2 and Mg-doped CeO_2 nanoparticles (Fig. 7). For the pure CeO_2 sample, the EDS spectrum reveals strong peaks corresponding to cerium (Ce) and oxygen (O), confirming the presence and purity of cerium oxide nanoparticles. The weight percentages of Ce and O were found to be 84.00% and 16.00%, respectively, while the atomic percentages were 37.47% for Ce and 62.53% for O. This confirms the stoichiometric formation of CeO_2.

Upon doping with magnesium, the EDS profile shows additional peaks corresponding to magnesium (Mg), along with Ce

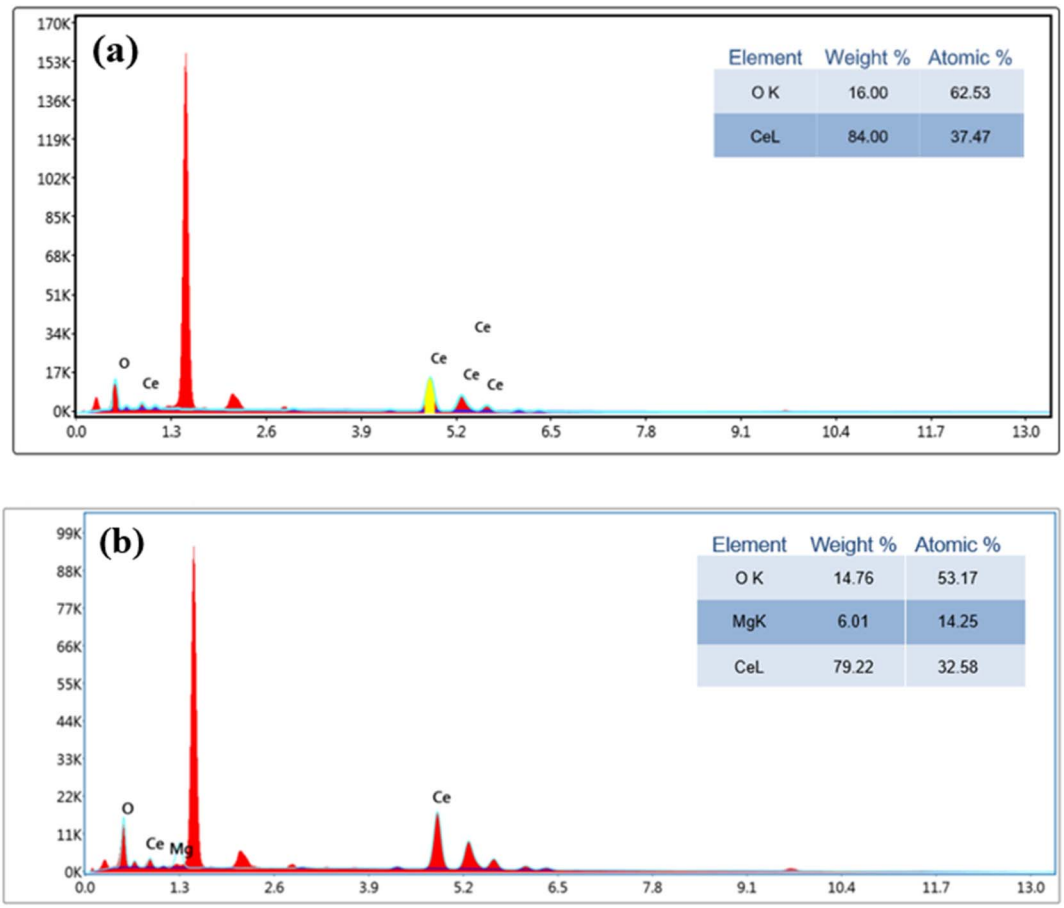

Fig. 7 EDX spectra of (a) CeO_2 NPs and (b) 6% Mg-doped CeO_2 NPs.

and O. The presence of Mg confirms the successful incorporation of the dopant into the CeO_2 matrix. In the Mg-doped CeO_2 sample, the weight percentages of Ce, O, and Mg were observed to be 79.22%, 14.76%, and 6.01%, respectively, with corresponding atomic percentages of 32.58%, 53.17%, and 14.25%. The decrease in Ce content and the appearance of Mg signals suggest that Mg has been effectively doped into the cerium oxide structure. Overall, the EDS analysis validates the elemental purity and successful doping process, supporting the structural and compositional integrity of the synthesized nanomaterials.

Elemental mapping of the 6% Mg-doped CeO_2 nanoparticles was performed using an energy-dispersive X-ray spectrometer (EDS) to confirm the presence and distribution of the constituent elements, cerium (Ce), oxygen (O), and magnesium (Mg) (Fig. 8). The combined mapping image (top left) clearly displays a uniform distribution of all three elements across the scanned area, indicating homogenous doping without agglomeration or phase segregation. The individual elemental maps further validate this observation: the Ce L (top right) and O K (bottom left) signals are densely and evenly spread throughout the matrix. The Mg K signal (bottom right), represented in purple, also shows a well-dispersed pattern, confirming the successful incorporation of Mg^{2+} ions into the CeO_2 lattice.

3.1.6. High-resolution transmission electron microscopy (HRTEM). The high-resolution images obtained from HRTEM analysis exhibit information regarding the size and shape of the synthesized 6% Mg-doped CeO_2 NPs. Fig. 9(a and b) show the HRTEM images with 100 nm and 5 nm resolutions, respectively. From these images, it can be seen that the 6% Mg-doped CeO_2

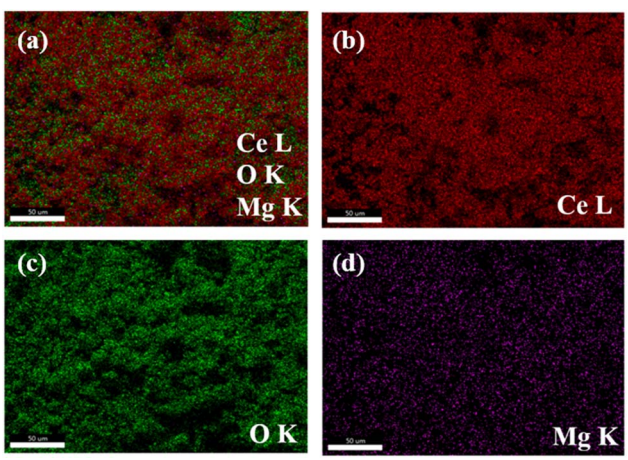

Fig. 8 Compositional elemental mapping of (a) homogeneously distributed Mg-doped CeO_2 NPs, (b) Ce, (c) O, and (d) Mg.

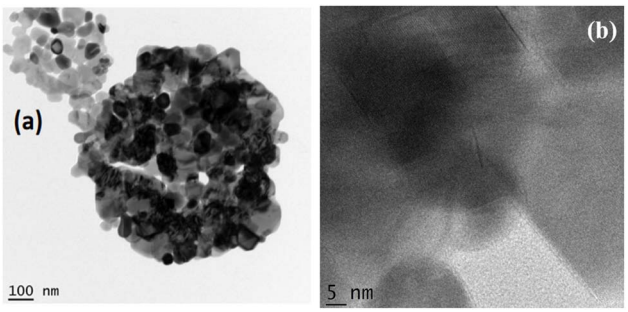

Fig. 9 HRTEM images of 6% Mg-doped CeO_2 NPs at different resolutions: (a) 200 nm and (b) 5 nm.

nanoparticles possess a quasi-spherical structure with a homogeneous particle size. The average particle size is about 25 nm, which shows that the nanoparticle synthesis has been efficiently controlled.

3.1.7. Brunauer–Emmett–Teller (BET) surface area analysis. The surface area of the synthesized nanoparticles was analyzed using nitrogen adsorption–desorption isotherms based on the Brunauer–Emmett–Teller (BET) method. The isotherms obtained for both samples are of Type IV with a hysteresis loop, characteristic of mesoporous materials. For the pure CeO_2 nanoparticles, the BET surface area was found to be 34 m^2 g^{-1} (Fig. 10(a)), whereas the Mg-doped CeO_2 nanoparticles showed a significantly increased surface area of 52 m^2 g^{-1} (Fig. 10(b)). This enhancement in surface area upon doping can be attributed to the incorporation of Mg^{2+} ions into the CeO_2 lattice, which introduces structural defects and inhibits grain growth, leading to the formation of smaller particles with a higher surface-to-volume ratio. The increase in surface area due to Mg doping plays a crucial role in enhancing the biological performance of the nanoparticles by providing more active sites and better interaction with target molecules.

3.1.8. Photoluminescence (PL). The photoluminescence (PL) spectra of pure CeO_2, MgO and 6% Mg-doped CeO_2 nanoparticles, as shown in Fig. 11(a), provide valuable insights into the optical behavior and defect structure of the synthesized materials. MgO NPs exhibit PL peaks at 422 nm and 397 nm, attributed to oxygen vacancies (F-centers) and surface defects, which produce emissions in the blue region of the visible spectrum. This positions MgO in the blue region of the CIE 1931 chromaticity diagram, making it suitable for blue-light-emitting applications. In contrast, CeO_2 and Mg-doped CeO_2 NPs exhibit two prominent emission peaks: one at 468 nm (blue region) and another at 633 nm (red region). These emissions are primarily attributed to the presence of oxygen vacancies, as well as the Ce^{3+}/Ce^{4+} redox transitions within the fluorite structure of cerium oxide.[47] The emission at 468 nm originates from electronic transitions involving oxygen vacancy-related defect states, where electrons from the conduction band recombine with trapped holes in these localized levels. The 633 nm emission is attributed to deeper defect levels or Ce^{3+}-to-Ce^{4+} charge transfer transitions. The presence of several small peaks alongside the prominent ones can be attributed to surface

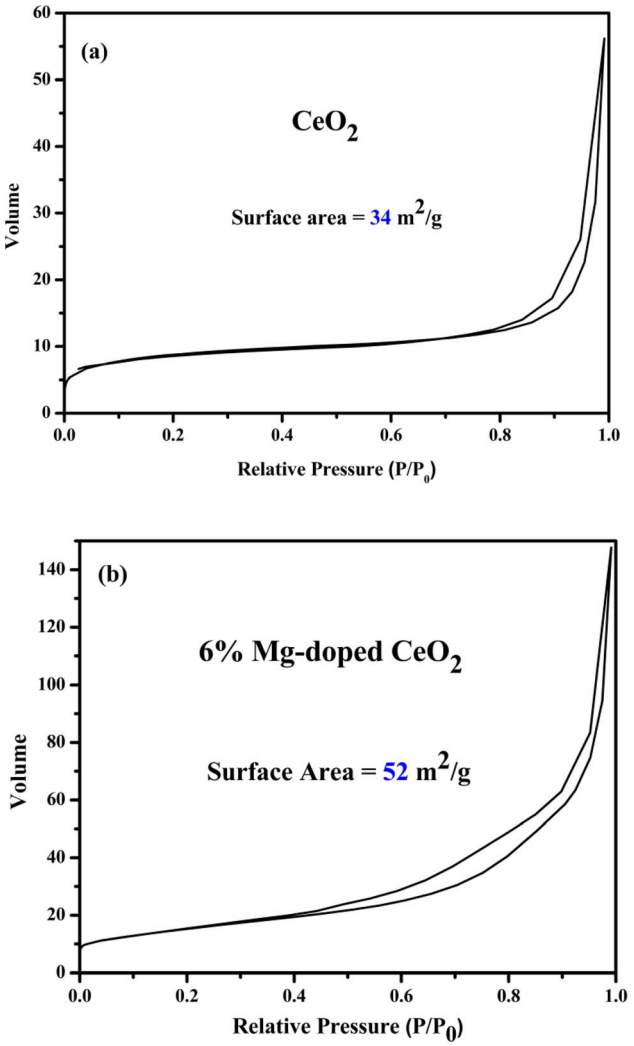

Fig. 10 BET images of (a) CeO_2 NPs and (b) 6% Mg-doped CeO_2 NPs.

defects, oxygen vacancies, and structural imperfections, which introduce localized states within the bandgap. Dopants or impurities may also create intermediate energy levels, enabling multiple emission pathways. Additionally, electron-phonon coupling can contribute to the fine structure observed near the main emission bands. Furthermore, the incorporation of Mg^{2+} ions (0.72 Å) in place of Ce^{4+} ions (1.01 Å) induces lattice distortions and generates additional oxygen vacancies due to charge imbalance, thereby enhancing the defect density. This increase in defect concentration alters the recombination dynamics of charge carriers, leading to enhanced visible-light emission in the doped samples.

The emitted light intensity was mapped as the chromaticity diagram (Fig. 11(b)). The combination of blue (468 nm) and red (633 nm) emissions places CeO_2 and Mg-doped CeO_2 NP samples near the white-light region on the CIE diagram, which demonstrates their potential use in optical and imaging applications.[48] These optical features are not only significant for display or imaging applications but also correlate with antibacterial performance. The presence of a high density of oxygen

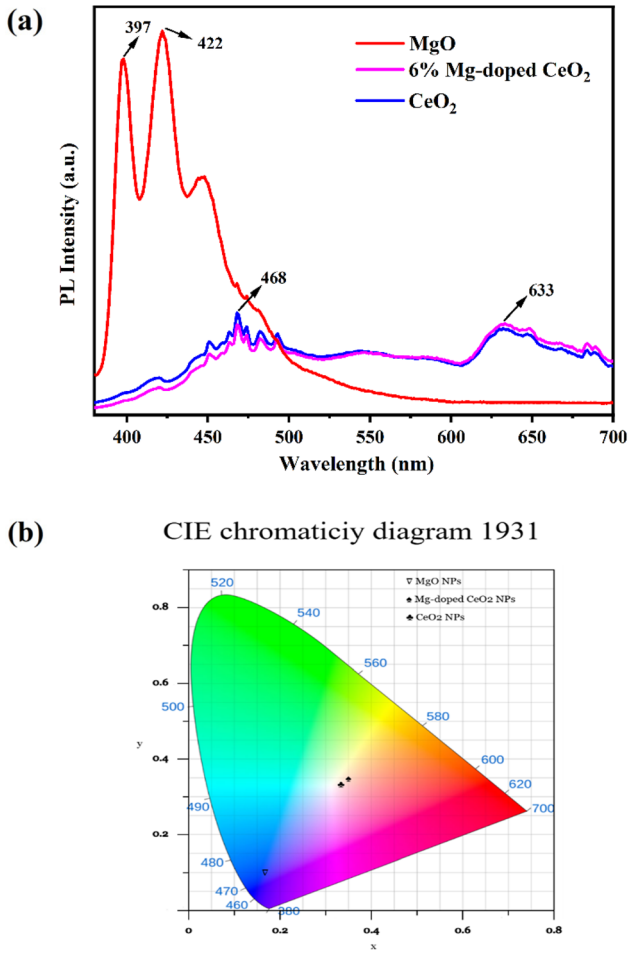

Fig. 11 (a) PL spectra, and (b) CIE 1931 chromaticity diagram of CeO_2 NPs, 6% Mg-doped CeO_2 NPs and MgO NPs.

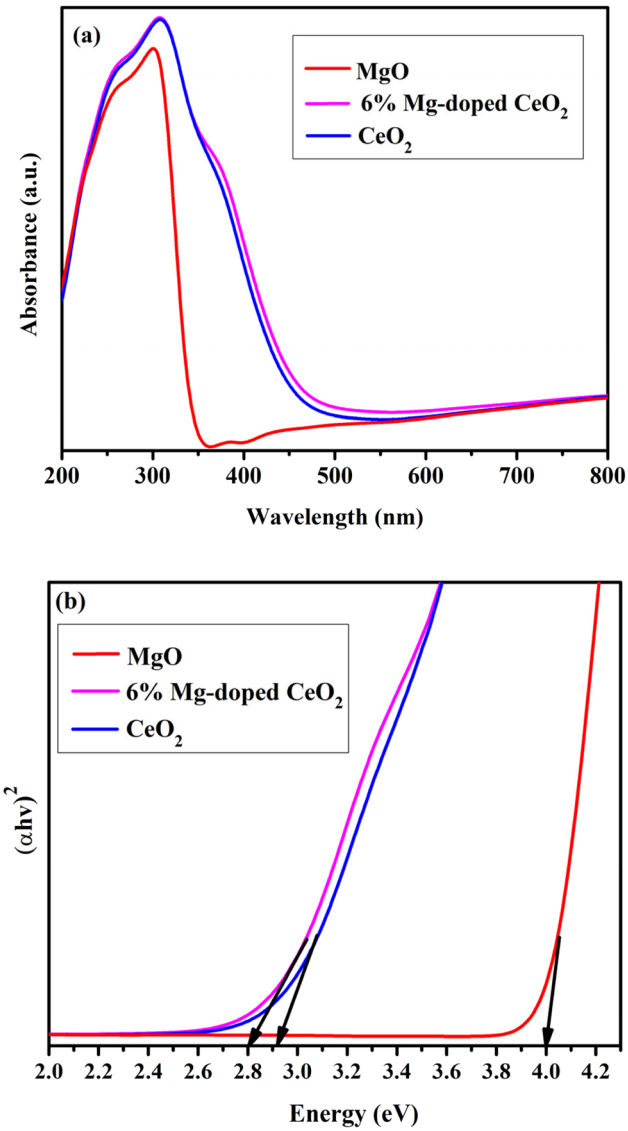

Fig. 12 (a) UV-VIS spectra and (b) Tauc plot of CeO_2 NPs, 6% Mg-doped CeO_2 NPs, and MgO NPs.

vacancies, indicated by strong PL emission, enhances the generation of reactive oxygen species (ROS) such as superoxide and hydroxyl radicals. These ROS play a pivotal role in disrupting bacterial membranes and inducing oxidative stress, thereby contributing to the antibacterial activity of the nanoparticles.

3.1.9. UV-visible spectroscopy. Fig. 12(a) displays the UV-Visible spectra of the synthesized CeO_2, MgO and 6% Mg-doped CeO_2 nanoparticles in the wavelength range of 200–800 nm. The absorption spectra revealed a prominent peak at 312 nm that is the characteristic peak of CeO_2 NPs, indicative of Ce–O bond formation, while MgO nanoparticles exhibit a distinct absorption peak around 295 nm, indicative of Mg–O bond formation. By employing the Tauc relation, the bandgap energies of the synthesized samples were determined using the following formula:

$$(\alpha h\nu)^2 = A\,(h\nu - E_g) \quad (6)$$

where α represents the absorption coefficient, $h\nu$ denotes the photon energy, E_g stands for the direct bandgap energy, and A is a constant. The band gap energies for CeO_2, Mg-doped CeO_2 NPs, and MgO NPs were determined by extrapolations of linear part of $(\alpha h\nu)^2$ *versus* energy plot, as shown in Fig. 12(b).[49,50] The bandgap energy of pure CeO_2 NPs was found to be 2.9 eV, which decreased to 2.8 eV upon doping with 6% Mg. This reduction in bandgap energy is attributed to the formation of oxygen vacancies and defect states induced by Mg incorporation. Such narrowing of the bandgap enhances the optical properties and reactive oxygen species (ROS) generation, contributing to improved antibacterial performance.[51] In contrast, the MgO nanoparticles exhibited a higher bandgap energy of 4.0 eV, consistent with their wide-bandgap semiconductor nature.

3.1.10. DLS. Dynamic light scattering (DLS) analyses were performed to determine the hydrodynamic diameter and zeta potential of the synthesized CeO_2, MgO, and Mg-doped CeO_2 nanoparticles (Fig. 13). The freshly synthesized CeO_2 nanoparticles exhibited a hydrodynamic diameter in the range of 133.3–148.9 nm, with an average size of 139.3 nm. Mg-doped

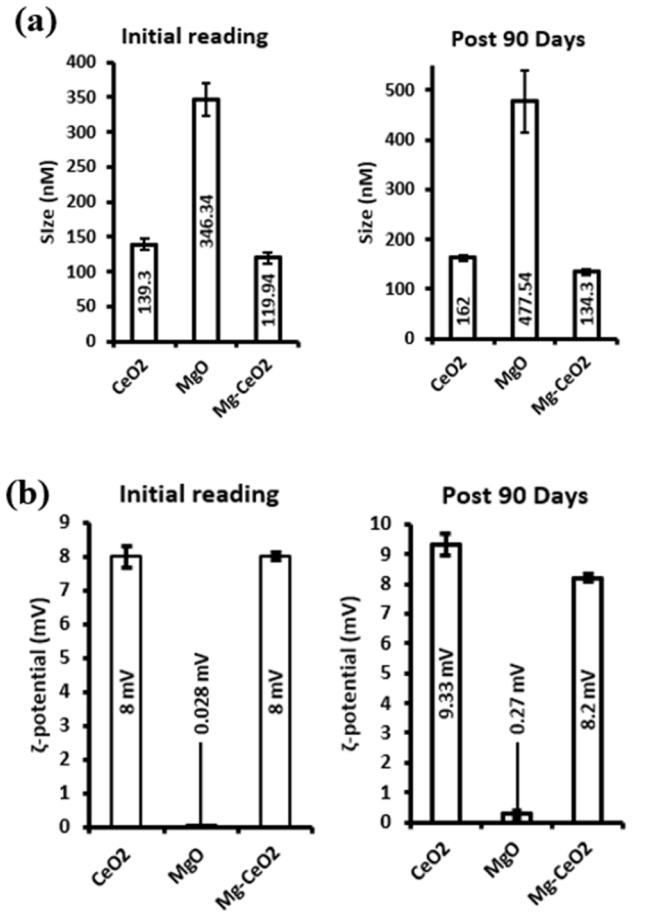

Fig. 13 Dynamic light scattering analyses: (a) hydrodynamic diameter and (b) zeta potential of the synthesized CeO_2, MgO and Mg-doped CeO_2 nanoparticles. Error bars represent the standard deviation; $n = 3$.

CeO_2 nanoparticles showed slightly smaller sizes (111.5–127.8 nm, average 119.9 nm), indicating improved aqueous dispersibility upon Mg doping. In contrast, MgO nanoparticles displayed significantly larger sizes (320.5–365.8 nm), confirming their tendency to agglomerate in an aqueous medium.

To assess the dispersion stability, the stored samples were analyzed again after 90 days at room temperature. The hydrodynamic size of CeO_2 NPs increased moderately to 162 nm, while Mg-doped CeO_2 NPs showed only a minimal increase to 134.3 nm, demonstrating excellent long-term colloidal stability. MgO NPs, however, exhibited a substantial increase to 477.5 nm, reflecting poor stability and pronounced agglomeration.

The initial zeta potentials of CeO_2 and Mg-doped CeO_2 NPs were 7.38–8.0 mV and 7.78–8.0 mV, respectively, whereas MgO NPs showed nearly neutral values (0.027–0.060 mV). After 90 days, CeO_2 and Mg-doped CeO_2 NPs retained stable positive zeta potentials of 9.33 mV and 8.2 mV, respectively, while MgO NPs remained close to neutral (0.27 mV).

These results confirm that Mg doping significantly enhances the colloidal stability of CeO_2 nanoparticles, with minimal aggregation and consistent hydrodynamic size and surface charge even after prolonged storage.

3.2. Mechanistic role of Mg in modulating CeO_2's properties

Specifically, substitution of Ce^{4+} (1.01 Å) by Mg^{2+} (0.72 Å) creates a charge imbalance that must be compensated to maintain lattice neutrality, primarily through the formation of oxygen vacancies. These vacancies introduce localized states within the band gap, which can trap or release charge carriers, thereby altering the electronic structure and enhancing the material's ability to generate reactive oxygen species. The increased oxygen vacancy concentration also promotes improved charge carrier mobility and surface reactivity, which may enhance electronic conductivity and antibacterial activity by facilitating electron transfer processes involved in oxidative stress mechanisms.[52] Furthermore, phytochemicals present in kiwi peel extract, especially polyphenols and flavonoids, possess multiple hydroxyl and carboxyl functional groups capable of chelating Ce^{4+} ions, forming intermediate metal–organic complexes that stabilize cerium species in the solution. Additionally, through redox mediation, these phytochemicals can donate electrons to reduce Ce^{4+} to Ce^{3+}, initiating the nucleation of cerium oxide nanoparticles. This biogenic reduction pathway not only drives the formation of nanostructured CeO_2 under mild conditions but also influences surface chemistry and defect distribution, which ultimately affect the material's functional performance.

3.3. Antibacterial activity analysis of Mg-doped CeO_2 NPs

The antibacterial activity of CeO_2, MgO, and Mg-doped CeO_2 nanoparticles was evaluated by determining their minimum inhibitory concentration (MIC) values against *Escherichia coli*, *Staphylococcus aureus*, and *Pseudomonas aeruginosa*. The MIC values are summarized in Table 1. Among the tested nanoparticles, Mg-doped CeO_2 NPs exhibited the most potent antibacterial activity, with MIC values of 62.5 μg mL^{-1} for *S. aureus* (MRSA) and 15.63 μg mL^{-1} for both *E. coli* and *P. aeruginosa*. In comparison, MgO nanoparticles showed moderate efficacy, with MIC values of 250 μg mL^{-1} for *S. aureus* (MRSA) and *P. aeruginosa*, and 125 μg mL^{-1} for *E. coli*. CeO_2 nanoparticles demonstrated the weakest antibacterial activity, with MIC values of 500 μg mL^{-1} for *S. aureus* (MRSA) and 250 μg mL^{-1} for both *E. coli* and *P. aeruginosa*. The variations in MIC values between Gram-positive and Gram-negative bacteria can be attributed to differences in cell wall composition, with slightly greater susceptibility concentration observed in *S. aureus*. The antibiotic control, kanamycin, exhibited the highest antibacterial efficacy, with MIC values of 12.5 μg mL^{-1} for *E. coli*, 3.12 μg mL^{-1} for *S. aureus*, and 1.563 μg mL^{-1} for *P. aeruginosa*.

Table 1 MIC data of nanomaterials and positive control kanamycin against *E. coli*, MRSA *S. aureus* and *P. aeruginosa* assessed by OD-based MIC determination assay

	MRSA	*E. coli*	*P. aeruginosa*
Cerium oxide	500 μg mL^{-1}	250 μg mL^{-1}	250 μg mL^{-1}
Magnesium oxide	250 μg mL^{-1}	125 μg mL^{-1}	250 μg mL^{-1}
Mg-doped CeO_2	62.5 μg mL^{-1}	15.63 μg mL^{-1}	15.63 μg mL^{-1}
Kanamycin	12.5 μg mL^{-1}	3.12 μg mL^{-1}	1.563 μg mL^{-1}

Table 2 Zone of inhibition data of nanomaterials and positive control kanamycin against *E. coli*, MRSA *S. aureus* and *P. aeruginosa* assessed by a well diffusion assay

	Kanamycin	Mg-doped CeO_2	MgO	CeO_2
E. coli	20 mm	15 mm	11 mm	7 mm
MRSA	14 mm	12 mm	8 mm	—
P. aeruginosa	22 mm	14 mm	10 mm	—

Although none of the nanoparticles matched the potency of kanamycin, the significantly lower MIC values of Mg-doped CeO_2 NPs compared to MgO and CeO_2 NPs highlight its potential as an effective antimicrobial agent. These findings suggest that Mg-doped CeO_2 nanoparticles could serve as promising alternatives or adjuncts to conventional antibiotics, especially in combating rising antibiotic resistance.

The antibacterial efficacy of Mg-doped CeO_2, CeO_2, and MgO nanoparticles was further evaluated using the well-diffusion assay, with kanamycin included as a positive control. The results, summarized in Table 2, were consistent with the MIC data, demonstrating that Mg-doped CeO_2 nanoparticles exhibited the highest antibacterial activity across all three tested strains. The zone of inhibition (ZOI) for Mg-doped CeO_2 nanoparticles was measured as 12 mm for *Staphylococcus aureus*, 15 mm for *Escherichia coli*, and 14 mm for *Pseudomonas aeruginosa*. In contrast, undoped CeO_2 nanoparticles showed a ZOI of only 7 mm against *E. coli*, with no visible inhibition observed for *S. aureus* (MRSA) and *P. aeruginosa*. Similarly, MgO nanoparticles displayed a lower antibacterial activity, with ZOI values of 11 mm for *E. coli*, 8 mm for *S. aureus* (MRSA), and 10 mm for *P. aeruginosa*, all of which were lower than that of Mg-doped CeO_2 NPs (Table 2, and Fig. 14(a–c)). These findings further support the enhanced antibacterial potential of Mg-doped CeO_2 nanoparticles over their individual metal oxide counterparts. The antibacterial activity of Mg-doped CeO_2 nanoparticles is primarily attributed to their ability to generate reactive oxygen species (ROS) and interact with bacterial membranes through surface defects and oxygen vacancies. The comparatively lower susceptibility of *Staphylococcus aureus* (a Gram-positive bacterium) relative to Gram-negative bacteria such as *Escherichia coli* and *Pseudomonas aeruginosa* can be explained by fundamental differences in cell wall structure, composition, and surface arrangements. Gram-negative bacteria possess a relatively thin peptidoglycan layer (~7–8 nm) located beneath an outer membrane composed of lipopolysaccharides (LPS). This outer membrane is readily accessible to nanoparticles and their released ions, facilitating more effective interactions with the bacterial membrane. Such interactions enhance cytotoxic effects, including oxidative stress and membrane disruption. In contrast, Gram-positive bacteria such as *S. aureus* feature a substantially thicker peptidoglycan layer (20–80 nm), embedded with teichoic and teichuronic acids.[64] This dense and rigid structure serves as a formidable physical barrier, limiting nanoparticle penetration and diffusion. The structurally weaker outer membrane of Gram-negative bacteria makes them more vulnerable to ROS-mediated oxidative damage and mechanical disruption caused by metal oxide nanoparticles.[65,66] These structural and biochemical differences account for the consistently greater susceptibility of Gram-negative bacteria in nanoparticle-based antimicrobial studies, highlighting the critical role of cell wall architecture in determining the nanoparticle efficacy. Among the tested materials, CeO_2 nanoparticles exhibited the lowest antibacterial activity compared to Mg-doped CeO_2 nanoparticles. Although CeO_2 nanoparticles is capable of generating reactive oxygen species (ROS) through its intrinsic redox behavior, its lower density of surface defects and oxygen vacancies, relative to Mg-doped CeO_2 nanoparticles, limits ROS generation. This reduced ROS production consequently reduces its antibacterial effectiveness.[67]

To better understand the antibacterial performance of the synthesized nanoparticles, a comparison with previously reported CeO_2-based nanomaterials is presented in Table 3. The Mg-doped CeO_2 nanoparticles exhibit comparable or enhanced antibacterial activity relative to other doped CeO_2 systems, which may be attributed to the synergistic effects of Mg doping, surface functionalization, and particle morphology.

3.4. Production of reactive oxygen species induced by Mg-doped CeO_2 NPs

To assess whether Mg-doped CeO_2 nanoparticles induce elevated oxidative stress in *S. aureus* (MRSA), ROS generation was analyzed using the fluorescent dye DCF-DA. Upon oxidation by reactive oxygen species such as superoxide ($O_2^{\bullet-}$) and

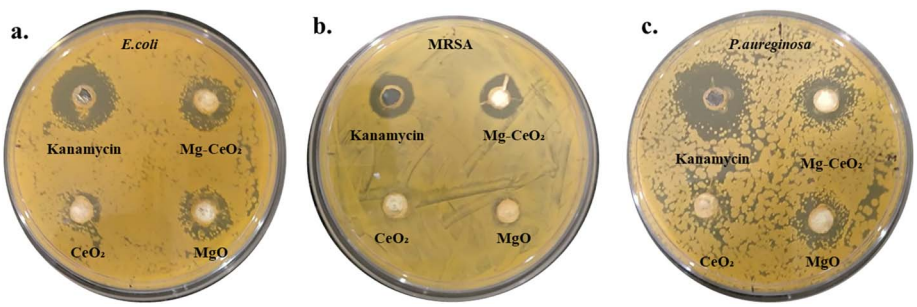

Fig. 14 Antibacterial assay of CeO_2, MgO, Mg-doped CeO_2 NPs (concentration = 100 μg mL^{-1}) and kanamycin (positive control; concentration = 50 μg mL^{-1}) post 24 h incubation: (a) *E. coli*, (b) *S. aureus* (MRSA) and (c) *P. aeruginosa*.

Table 3 Comparative antibacterial activity of Mg-doped CeO_2 nanoparticles with those of the previously reported CeO_2-based nanomaterials

Nanomaterial	Microorganism tested	Zone of inhibition (mm)	Concentration used	Synthesis method	Reference
Ag–CeO_2 NPs Au–CeO_2 NPs	*S. aureus*, *E. coli*	26 mm, 30 mm 25 mm, 28 mm	100 mg mL^{-1}	Green synthesis (*Justicia adhatoda* leaves)	53
CeO_2 NPs	*E. coli*, *B. subtilis*	1.7 cm, 1.8 cm	100 mg mL^{-1}	Green synthesis (tannic acid)	54
CeO_2 NPs	*E. coli*, *P. aeruginosa*, *S. saprophyticus* and *Bacillus subtilis*	23 mm, 21 mm, 21 mm, 20 mm	100 μg mL^{-1}	Green synthesis (*Calotropis procera* flower)	55
CeO_2 NPs	*S. aureus*, *K. pneumonia*	21 mm, 19 mm	30 μg mL^{-1}	Green synthesis (*Abelmoschus esculentus*)	56
Ag/CeO_2 NPs	*E. coli*, *S. aureus*	13 mm, 12 mm	100 μg mL^{-1}	Green synthesis (*Morinda tinctoria*)	57
CeO_2 NPs	*E. coli*, *S. typhimurium*, *L. monocytogenes*, *S. aureus*, *B. cereus*	9 mm, 12 mm, 10 mm, 5 mm, 7 mm	50 μg mL^{-1}	Wet chemical synthesis	58
Zr-doped CeO_2 NPs	*S. aureus*, *E. coli*, *P. aeruginosa*, *S. fecalis*, *B. subtilis*, *P. vulgaris*	11 mm, 7 mm, 9 mm, 8 mm, 8 mm, 9 mm	_	Co-precipitation	59
Nd-doped CeO_2 NPs	*E. coli*, *S. aureus*	16 mm, 20 mm	450 μg mL^{-1} 500 μg mL^{-1}	Solid-state reaction	60
Ba-doped CeO_2 NPs	*S. mutans* and *S. aureus*	7 mm, 6 mm	2 mg mL^{-1}	Co-precipitation	61
Y-doped CeO_2 NPs	*P. aeruginosa*, *C. diphtheria*	15.5 mm, 15 mm	500 μg mL^{-1}	Chemical precipitation	62
Mn-doped CeO_2 NPs	*E. coli*	8.5 mm	400 μg mL^{-1}	Soft chemical route	63
Zr-doped CeO_2 NPs	*S. aureus*, *E. coli*, *P. aeruginosa*	11 mm, 7 mm, 6 mm	—	Co-precipitation	75
Mg-doped CeO_2 NPs	Methicillin-resistant *S. aureus*, *E. coli*, *P. aeruginosa*	12 mm, 15 mm, 14 mm	100 μg mL^{-1}	Green synthesis (*Actinidia deliciosa* peel)	Present study

hydroxyl radicals ($^{\bullet}OH$), DCF-DA is converted into dichlorodihydrofluorescein (DCFH), which emits green fluorescence. As shown in Fig. 15, untreated bacterial cells exhibited no detectable green fluorescence, indicating the absence of ROS generation and oxidative stress under control conditions. In contrast, both CeO_2 and Mg-doped CeO_2 NP-treated cells demonstrated increased ROS production, shown by the presence of green fluorescence. Notably, cells treated with Mg-doped CeO_2 NPs showed significantly higher fluorescence intensity than those treated with CeO_2 NPs at both tested concentrations (50 μg mL^{-1} and 100 μg mL^{-1}), indicating greater ROS generation. These results indicate that Mg-doped CeO_2 NPs induce more pronounced oxidative stress in *S. aureus* (MRSA), probably contributing to its enhanced antibacterial activity.

The enhanced ROS generation activity of Mg-doped CeO_2 NPs is attributed to the synergistic effects of magnesium doping, which increases the density of oxygen vacancies and structural defects within the CeO_2 crystal lattice. The substitution of Ce^{4+} ions (ionic radius: 1.01 Å) with smaller Mg^{2+} ions (ionic radius: 0.72 Å) induces lattice distortions (eqn (7)), promoting enhanced redox cycling between Ce^{3+} and Ce^{4+} states. The generated structural defects and oxygen vacancies serve as active sites for the formation of reactive oxygen species (ROS), including superoxide anions ($O_2^{\bullet-}$) and hydroxyl radicals ($^{\bullet}OH$) (eqn (8) and (9)). These ROS species contribute to antibacterial activity by disrupting bacterial membrane integrity and inducing oxidative damage to vital intracellular components, ultimately leading to bacterial cell death.[63,68–70] Probable mechanism of ROS generation can be stated as follows:

$$MgO + 2CeO_2 \rightarrow Mg''_{Ce} + V^{\cdot\cdot}_{O} + 2Ce^{3+} + O_2; \quad (7)$$

where $V^{\cdot\cdot}_{O}$ represents oxygen vacancies and Mg''_{Ce} denotes that Mg occupies the lattice site of Ce with $''$ indicating a net double-negative charge in the Kröger–Vink notation.

$$Ce^{3+} + O_2 \rightarrow Ce^{4+} + O_2^{\bullet-}; \quad (8)$$

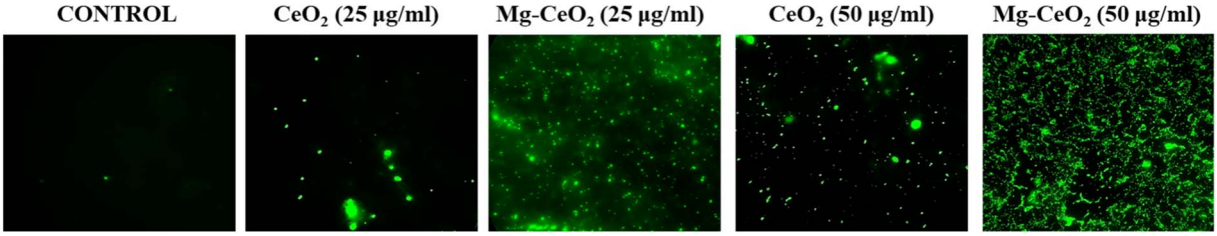

Fig. 15 Intracellular ROS generation measured using fluorescence microscopy of MRSA treated with CeO_2 NPs and Mg-doped CeO_2 NPs at different concentrations (25 μg mL^{-1} and 50 μg mL^{-1}).

$$Ce^{3+} + H_2O_2 \rightarrow Ce^{4+} + {}^{\cdot}OH + OH^{-} \quad (9)$$

In contrast, CeO_2 nanoparticles exhibited lower antibacterial efficacy, primarily due to their limited capacity for ROS generation compared to Mg-doped CeO_2 nanoparticles. These findings support the conclusion that magnesium doping enhances ROS production, thereby significantly improving the antibacterial activity of the nanoparticles.

3.5. Morphological analysis of bacterial cell damage induced by Mg-doped CeO_2 NPs

Scanning electron microscopy (SEM) analysis revealed significant morphological alterations in bacterial cell morphology treated with Mg-doped CeO_2 nanoparticles, as compared to untreated controls. Untreated *S. aureus*, *E. coli*, and *P. aeruginosa* cells exhibited intact structures with smooth, undisturbed cell membranes (Fig. 16). In contrast, cells treated with Mg-doped CeO_2 nanoparticles showed extensive membrane disruption, characterized by visible ruptures, cell shrinkage, and the formation of surface perforations (Fig. 16(d–f)). These structural deformities are indicative of severe cellular damage and suggest a bactericidal mode of action for Mg-doped CeO_2 nanoparticles. The observed morphological changes provide direct evidence of the nanoparticles' ability to compromise bacterial membrane integrity, ultimately leading to bacterial cell death.

3.6. Biofilm inhibition activity of Mg-doped CeO_2 NPs

Biofilm inhibition assays were conducted to evaluate the antibiofilm efficacy of Mg-doped CeO_2 nanoparticles. The ability of methicillin-resistant *Staphylococcus aureus* (MRSA) to form biofilms poses significant clinical and biomedical challenges due to increased resistance to antimicrobial agents and evasion of host immune responses. Biofilms are structured communities of bacterial cells embedded within a self-produced extracellular polymeric substance (EPS), which provides a protective barrier against environmental stresses.[71] In this study, Mg-doped CeO_2 nanoparticles demonstrated significant biofilm inhibition activity against *S. aureus* (MRSA). As shown in Fig. 17, treatment with Mg-doped CeO_2 nanoparticles at concentrations of 25 μg mL^{-1}, 50 μg mL^{-1}, and 100 μg mL^{-1} resulted in approximately 60%, 80%, and 85% reduction in biofilm biomass, respectively. In contrast, lower concentrations (5 μg mL^{-1} and 15 μg mL^{-1}) were ineffective in significantly reducing biofilm formation. These findings indicate that Mg-doped CeO_2 nanoparticles, at specific concentrations, effectively inhibit biofilm development against *S. aureus* (MRSA). The observed antibiofilm activity suggests that Mg-doped CeO_2 nanoparticles could potentially enhance its own antibacterial efficacy by reducing biofilm-associated resistance.

3.7. Potential mechanism of antibacterial activity

The antibacterial mechanism of Mg-doped CeO_2 nanoparticles is multifaceted, involving both physical disruption and biochemical interactions. Scanning electron microscopy (SEM) analysis revealed substantial membrane damage in bacterial cells treated with Mg-doped CeO_2 nanoparticles, indicating that

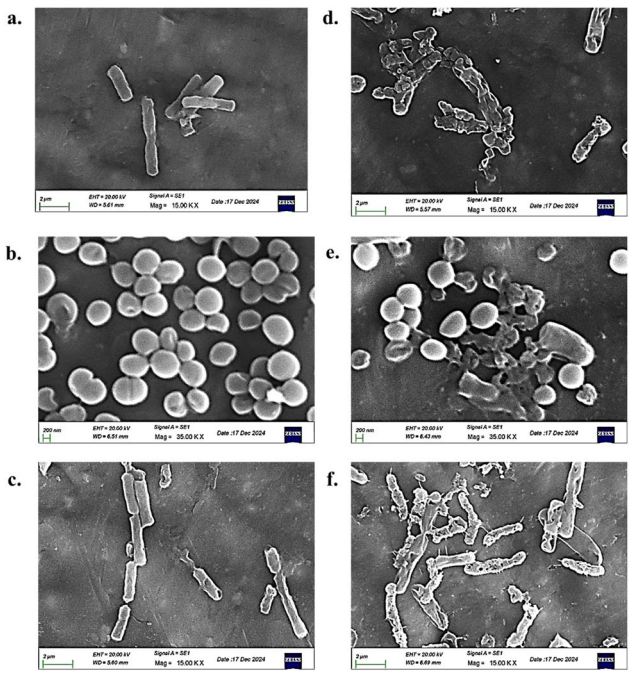

Fig. 16 SEM analysis of *E. coli*: (a) control and (d) treated with Mg-doped CeO_2 NPs. SEM analysis of *S. aureus* (MRSA): (b) control and (e) treated with Mg-doped CeO_2 NPs. SEM analysis of *P. aeruginosa*: (c) control and (f) treated with Mg-doped CeO_2 NPs post 12 h incubation.

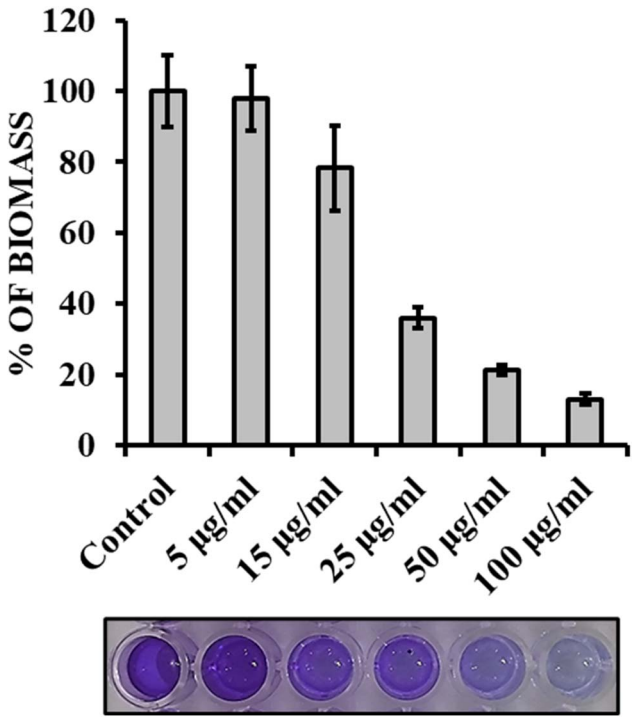

Fig. 17 Crystal violet assay: biofilm inhibition activity of Mg-doped CeO_2 NPs at different concentrations of 5 μg mL^{-1}, 15 μg mL^{-1}, 25 μg mL^{-1}, 50 μg mL^{-1}, and 100 μg mL^{-1} evaluated against MRSA (bar graph depicts the mean of triplicate samples). Bottom panel shows the crystal violet stained plates of the respective concentrations.

physical disruption of the cell membrane is a primary mode of antibacterial action. The synthesized nanoparticles exhibited crystallite sizes of 5–6 nm, particle sizes around 25 nm, and larger agglomerates in the range of 45–60 nm. The smaller crystallites provide a high surface area and more defect sites, which facilitate greater reactive oxygen species (ROS) production. Particles around 25 nm are suitably sized for close interaction with bacterial membranes, allowing localized ROS buildup. Meanwhile, larger aggregates enhance membrane contact and may exert physical stress, contributing to membrane disruption. These combined, size-dependent effects significantly strengthen the overall antibacterial activity. The physicochemical factors including nanoparticle size, shape, surface charge and the degree of oxidative stress play critical roles in antibacterial activity. In this study, oxidative stress was considered as the mechanism of action, primarily attributed to the increased Ce^{3+}/Ce^{4+} redox cycling ratio, which facilitates enhanced ROS generation, post interaction between positively charged Mg-doped CeO_2 NPs and negatively charged bacterial cell membrane. This finding shows that the antibacterial activity of these nanoparticles depends on surface charge and also their capacity to produce high levels of ROS. The observed membrane disruption probably results from direct interactions between nanoparticles and the bacterial cell membrane, leading to the loss of structural integrity, leakage of intracellular contents, and eventual cell death (Fig. 18). The cell membrane disruption and generation of oxidative stress within bacterial cells eventually leads to damage on critical cellular components such as proteins and DNA.[72–74] Magnesium doping alters the electronic structure and surface reactivity of CeO_2, leading to increased reactive oxygen species (ROS) generation and enhanced antibacterial activity. The combined effects of membrane disruption and ROS production indicate a synergistic antimicrobial response of Mg-doped CeO_2 nanoparticles against both Gram-positive and Gram-negative bacteria. This multi-targeted mechanism suggests potential antimicrobial efficacy, as it affects multiple cellular components and interferes with essential translational processes. The broader and less specific mechanism of Mg-doped CeO_2 nanoparticles thus offers a strategic advantage, potentially making them an effective antimicrobial agent.

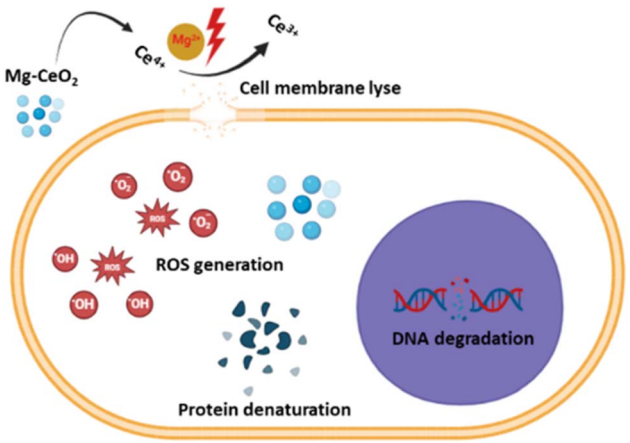

Fig. 18 Mechanism of antibacterial activity of Mg-doped CeO_2 NPs.

4. Conclusions

In this study, CeO_2 and Mg-doped CeO_2 nanoparticles synthesized by the green sol–gel method using kiwi peel extract demonstrated significant antibacterial activity against *E. coli*, *S. aureus*, and *P. aeruginosa*. The successful formation and structural integrity of the synthesized nanoparticles were validated by characterization techniques including XRD, FTIR spectroscopy, FESEM, HRTEM, BET, Raman spectroscopy, PL spectroscopy, and UV-Vis spectroscopy. Mg-doped CeO_2 nanoparticles exhibited the lowest minimum inhibitory concentration (MIC) values 15.63 μg mL^{-1} for both *Escherichia coli* and *Pseudomonas aeruginosa*, and 62.5 μg mL^{-1} for *Staphylococcus aureus* along with the zones of inhibition measuring 15 mm, 14 mm, and, 12 mm, respectively. The enhanced antibacterial activity is primarily attributed to increased ROS generation, facilitated by a higher density of oxygen vacancies and efficient Ce^{3+}/Ce^{4+} redox cycling. This was further confirmed by ROS assays, which demonstrated that Mg-doped CeO_2 NPs produced significantly greater oxidative stress than that of undoped CeO_2 NPs. Morphological analysis by scanning electron microscopy (SEM) revealed extensive structural damage in bacterial cells treated with Mg-doped CeO_2 nanoparticles, including ruptured membranes, cell shrinkage, and surface perforations. In addition to its antibacterial action, Mg-doped CeO_2 nanoparticles also exhibited strong biofilm inhibition activity against *S. aureus* (MRSA), further supporting its broad-spectrum antimicrobial potential. Collectively, these findings highlight the potential of Mg-doped CeO_2 nanoparticles as effective antibacterial agents, especially for combating antimicrobial resistant strains.

Author contributions

Nibedita Nayak: conceptualization, methodology, writing. Uday Suryakanta: methodology, writing. Swatilekha Das: methodology. Dindyal Mandal: editing, review. Tapas Ranjan Sahoo: supervision, project administration, review and editing.

Conflicts of interest

There are no conflicts to declare.

Data availability

Data will be made available on request.

References

1 A. A. Roy, S. Mutalik and N. Dhas, *Int. J. Biol. Macromol.*, 2024, **278**, 134977.
2 J. L. Brower, *Microb. Ecol.*, 2018, **76**, 19–36.
3 S. Rehman, *J. Infect. Public Health*, 2023, **16**, 611–617.

4 K. Zawadzka, P. Bernat, A. Felczak, S. Różalska and K. Lisowska, *Int. J. Antimicrob. Agents*, 2018, **51**, 458–467.
5 T. Picoli, C. M. Peter, J. L. Zani, S. B. Waller, M. G. Lopes, K. N. Boesche, S. O. Hübner and G. Fischer, *Microb. Pathog.*, 2017, **112**, 57–62.
6 W. Y. Belay, M. Getachew, B. A. Tegegne, Z. H. Teffera, A. Dagne, T. K. Zeleke, R. B. Abebe, A. A. Gedif, A. Fenta, G. Yirdaw and A. Tilahun, *Front. Pharmacol*, 2024, **15**, 1444781.
7 Ç. Yılmaz and G. Özcengiz, *Biochem. Pharmacol.*, 2017, **133**, 43–62.
8 Í. R. Garcia, F. A. de Oliveira Garcia, P. S. Pereira, H. D. M. Coutinho, A. Siyadatpanah, R. Norouzi, P. Wilairatana, M. de Lourdes Pereira, V. Nissapatorn, S. R. Tintino and F. F. G. Rodrigues, *Life Sci.*, 2022, **295**, 120391.
9 C. R. Arciola, D. Campoccia, S. Ravaioli and L. Montanaro, *Front. Cell. Infect. Microbiol.*, 2015, **5**, 7.
10 R. Alenazy, *Biology*, 2022, **11**, 1328.
11 I. O. Pandeya, O. Alegun and Y. Wei, *ACS Infect. Dis.*, 2020, **6**, 2337–2354.
12 L. de Nies, C. M. Kobras and M. Stracy, *Nat. Rev. Microbiol.*, 2023, **21**, 789–804.
13 J. Yang, L. Du, J. Guo, L. Zhang, S. Wang and X. Wang, *Int. J. Biol. Macromol.*, 2025, **308**, 142572.
14 S. Xiang, H. Zhang, J. Zhang, X. Li, X. Lin and W. Sun, *Int. J. Pharm. X*, 2025, **10**, 100400.
15 S. Rahman, S. Sadaf, M. E. Hoque, A. Mishra, N. M. Mubarak, G. Malafaia and J. Singh, *RSC Adv.*, 2024, **14**, 13862–13899.
16 B. Priyadarshini, T. Patra and T. R. Sahoo, *J. Magnes. Alloys*, 2021, **9**, 478–488.
17 T. R. Sahoo, M. Armandi, R. Arletti, M. Piumetti, S. Bensaid, M. Manzoli, S. R. Panda and B. Bonelli, *Appl. Catal. B Environ.*, 2017, **211**, 31–45.
18 E. Casals, M. Zeng, M. Parra-Robert, G. Fernández-Varo, M. Morales-Ruiz, W. Jimenez, V. Puntes and G. Casals, *Small*, 2020, **16**, 1907322.
19 M. S. Lord, J. F. Berret, S. Singh, A. Vinu and A. S. Karakoti, *Small*, 2021, **17**, 2102342.
20 H. Ruan, S. Zhang, H. Wang, J. Pei, R. Zhao, X. Mu, H. Wang and X. Zhang, *ACS Appl. Nano Mater.*, 2022, **5**, 6564–6574.
21 G. Xiao, H. Li, Y. Zhao, H. Wei, J. Li and H. Su, *ACS Appl. Nano Mater.*, 2022, **5**, 14147–14170.
22 S. Chahal, L. Phor, S. Singh, A. Singh, J. Malik, P. Goel, A. Kumar, S. Kumar and P. Kumar, *Ceram. Int.*, 2022, **48**, 28961–28968.
23 S. K. Alla, R. K. Mandal and N. K. Prasad, *RSC Adv.*, 2016, **6**, 103491–103498.
24 N. Sezer, Z. Evis, S. M. Kayhan, A. Tahmasebifar and M. Koç, *J. Magnes. Alloys*, 2018, **6**, 23–43.
25 Z. Huang, P. Rajasekaran, A. Ozcan and S. Santra, *J. Agric. Food Chem.*, 2018, **66**, 8679–8686.
26 M. Chinthala, A. Balakrishnan, P. Venkataraman, V. Manaswini Gowtham and R. K. Polagani, *Environ. Chem. Lett.*, 2021, **19**, 4415–4454.
27 S. N. Matussin, M. H. Harunsani and M. M. Khan, *J. Rare Earths*, 2023, **41**, 167–181.
28 C. Dhand, N. Dwivedi, X. J. Loh, A. N. J. Ying, N. K. Verma, R. W. Beuerman, R. Lakshminarayanan and S. Ramakrishna, *RSC Adv.*, 2015, **5**, 105003–105037.
29 M. Rani, J. Yadav, S. Chaudhary and U. Shanker, *J. Environ. Chem. Eng.*, 2021, **9**, 106763.
30 V. Soni, P. Raizada, P. Singh, H. N. Cuong, S. Rangabhashiyam, A. Saini, R. V. Saini, Q. Van Le, A. K. Nadda, T. T. Le and V. H. Nguyen, *Environ. Res.*, 2021, **202**, 111622.
31 R. Mohammadinejad, S. Karimi, S. Iravani and R. S. Varma, *Green Chem.*, 2016, **18**, 20–52.
32 S. Dubey, T. Virmani, S. K. Yadav, A. Sharma, G. Kumar and A. Alhalmi, *J. Nanomater.*, 2024, **2024**, 9914079.
33 S. N. Naidi, M. H. Harunsani, A. L. Tan and M. M. Khan, *J. Mater. Chem. B*, 2021, **9**, 5599–5620.
34 N. Nayak, U. Suryakanta, D. Mandal and T. R. Sahoo, *ChemistrySelect*, 2024, **9**, e202402964.
35 Y. S. Khadar, A. Balamurugan, V. P. Devarajan, R. Subramanian and S. D. Kumar, *J. Mater. Res. Technol.*, 2019, **8**, 267–274.
36 P. Maleki, F. Nemati, A. Gholoobi, A. Hashemzadeh, Z. Sabouri and M. Darroudi, *Inorg. Chem. Commun.*, 2021, **131**, 108762.
37 A. Norbert, S. M. Alappatt, S. S. John, S. Shaji, S. K. Remillard, U. P. Deshpande and R. Reena Philip, *Phys. Status Solidi A*, 2023, **220**, 2200731.
38 D. Satpal, J. Kaur, V. Bhadariya and K. Sharma, *J. Food Process. Preserv.*, 2021, **45**, e15588.
39 E. Gomathi, M. Jayapriya and M. Arulmozhi, *Inorg. Chem. Commun.*, 2021, **130**, 108670.
40 D. Bharathi, J. Lee, P. Karthiga, R. Mythili, S. Devanesan and M. S. AlSalhi, *Waste Biomass Valoriz.*, 2024, **15**, 1859–1868.
41 V. Sanz, L. López-Hortas, M. D. Torres and H. Domínguez, *Trends Food Sci. Technol.*, 2021, **107**, 401–414.
42 N. Gugala, D. Vu, M. D. Parkins and R. J. Turner, *Antibiotics*, 2019, **8**, 51.
43 J. Teng, S. Imani, A. Zhou, Y. Zhao, L. Du, S. Deng, J. Li and Q. Wang, *Biomed. Pharmacother.*, 2023, **167**, 115564.
44 T. Lohitha and H. M. Albert, *J. Fluoresc.*, 2024, 1–14, DOI: 10.1007/s10895-024-03831-5.
45 K. Kumari, R. N. Aljawfi, A. K. Chawla, R. Kumar, P. A. Alvi, A. Alshoaibi, A. Vij, F. Ahmed, M. Abu-Samak and S. Kumar, *Ceram. Int.*, 2020, **46**, 7482–7488.
46 R. Munirathnam, H. C. Manjunatha, Y. S. Vidya, L. Seenappa, K. N. Sridhar, T. C. Sabari Girisun, T. Sharmila and S. Veera Rethina Murugan, *Phys. B Condens. Matter.*, 2025, **711**, 417226.
47 J. Saranya, K. S. Ranjith, P. Saravanan, D. Mangalaraj and R. T. R. Kumar, *Mater. Sci. Semicond. Process.*, 2014, **26**, 218–224.
48 J. C. Rhoda, D. Pourkodee, J. P. Suchitra, M. Giruba, H. M. Albert and C. A. Gonsago, *BioNanoScience*, 2025, **15**, 1–16.
49 J. C. Rhoda, S. Chellammal, H. M. Albert, K. Ravichandran and C. A. Gonsago, *J. Fluoresc.*, 2024, **34**, 587–598.

50 H. M. Albert, G. Durgadevi, D. Kanimozhi and C. A. Gonsago, *Appl. Phys. A*, 2024, **130**, 543.
51 K. Dubey, S. Dubey, V. Sahu, A. Modi, J. Bamne, F. Z. Haque and N. K. Gaur, *Mater. Sci. Eng., B*, 2023, **288**, 116154.
52 S. N. Matussin, F. Khan, M. H. Harunsani, Y. M. Kim and M. M. Khan, *ACS Omega*, 2023, **8**, 11868–11879.
53 P. Nithya and M. Sundrarajan, *J. Photochem. Photobiol. B Biol.*, 2020, **202**, 111706.
54 K. M. Kumar, M. Mahendhiran, M. C. Diaz, N. Hernandez-Como, A. Hernandez-Eligio, G. Torres-Torres, S. Godavarthi and L. M. Gomez, *Mater. Lett.*, 2018, **214**, 15–19.
55 A. Muthuvel, M. Jothibas, V. Mohana and C. Manoharan, *Inorg. Chem. Commun.*, 2020, **119**, 108086.
56 H. E. Ahmed, Y. Iqbal, M. H. Aziz, M. Atif, Z. Batool, A. Hanif, N. Yaqub, W. A. Farooq, S. Ahmad, A. Fatehmulla and H. Ahmad, *Molecules*, 2021, **26**, 4659.
57 A. Ahmad, M. S. Javed, S. Khan, T. M. Almutairi, A. A. Mohammed and R. Luque, *Chemosphere*, 2023, **310**, 136841.
58 O. L. Pop, A. Mesaros, D. C. Vodnar, R. Suharoschi, F. Tăbăran, L. Mageruşan, I. S. Tódor, Z. Diaconeasa, A. Balint, L. Ciontea and C. Socaciu, *Nanomaterials*, 2020, **10**, 1614.
59 R. Bakkiyaraj, M. Balakrishnan, G. Bharath and N. Ponpandian, *J. Alloys Compd.*, 2017, **724**, 555–564.
60 A. Karmakar, S. Samanta, S. Chattopadhyay, J. Banerjee, M. Nath, B. J. Sarkar, D. Raha, S. Mitra, S. Sarkar, S. K. Dash and A. Bandyopadhyay, *Chem. Phys. Impact*, 2023, **7**, 100337.
61 N. Sisubalan, C. Karthikeyan, V. S. Kumar, K. Varaprasad, R. Vanajothi and R. Sadiku, *RSC Adv.*, 2021, **11**, 30623–30634.
62 K. Vignesh, D. Sivaganesh, S. Saravanakumar and M. P. Rani, *Mater. Today Proc.*, 2022, **65**, 127–145.
63 M. Atif, S. Iqbal, M. Fakhar-E-Alam, M. Ismail, Q. Mansoor, L. Mughal, Q. Mansoor, L. Mughal, M. H. Aziz, A. Hanif and W. A. Farooq, *BioMed Res. Int.*, 2019, **2019**, 7156828.
64 K. M. Kumar, M. Mahendhiran, M. C. Diaz, N. Hernandez-Como, A. Hernandez-Eligio, G. Torres-Torres, S. Godavarthi and L. M. Gomez, *Mater. Lett.*, 2018, **214**, 15–19.
65 N. S. Ahmad, N. Abdullah and F. M. Yasin, *Toxicol Rep*, 2020, **7**, 693–699.
66 Y. N. Slavin, J. Asnis, U. O. Hńfeli and H. Bach, *J. Nanobiotechnol.*, 2017, **15**, 1–20.
67 T. V. Surendra and S. M. Roopan, *J. Photochem. Photobiol. B Biol.*, 2016, **161**, 122–128.
68 J. L. Tang, S. S. Moonshi and H. T. Ta, *Cell. Mol. Life Sci.*, 2023, **80**, 46.
69 Y. Bai, Y. Li, Y. Li and L. Tian, *ACS Omega*, 2024, **9**, 8601–8614.
70 T. Lohitha and H. M. Albert, *J. Mater. Res.*, 2025, **40**, 1279–1291.
71 A. Kaushik, H. Kest, M. Sood, B. W. Steussy, C. Thieman and S. Gupta, *Pathogens*, 2024, **13**, 76.
72 S. Pansambal, R. Oza, S. Borgave, A. Chauhan, P. Bardapurkar, S. Vyas and S. Ghotekar, *Appl. Nanosci.*, 2023, **13**, 6067–6092.
73 Z. R. Tóth, A. Feraru, G. Veréb, D. C. Vodnar, M. Todea, A. Timar-Gabor, A. K. Dave, D. Sand, A. Dreanca, K. Magyari and L. Baia, *Biomater. Adv.*, 2025, **171**, 214229.
74 L. J. Su, J. H. Zhang, H. Gomez, R. Murugan, X. Hong, D. Xu, F. Jiang and Z. Y. Peng, *Oxid. Med. Cell. Longev.*, 2019, **2019**, 5080843.
75 R. Bakkiyaraj, M. Balakrishnan, G. Bharath and N. Ponpandian, *J. Alloys Compd.*, 2017, **724**, 555–564.